Theses and Dissertations

2013

Design of microwave front-end narrowband filter and limiter components

Lee W. Cross
The University of Toledo

Follow this and additional works at: http://utdr.utoledo.edu/theses-dissertations

A Dissertation

entitled

Design of Microwave Front-End Narrowband Filter and Limiter Components

by

Lee W. Cross

Submitted to the Graduate Faculty as partial fulfillment of the requirements for the

Doctor of Philosophy Degree in Engineering

_____
Vijay Devabhaktuni, Ph.D., Committee Chair

_____
Mansoor Alam, Ph.D., Committee Member

_____
Mohammad Almalkawi, Ph.D., Committee Member

_____
Matthew Franchetti, Ph.D., Committee Member

_____
Daniel Georgiev, Ph.D., Committee Member

_____
Telesphor Kamgaing, Ph.D., Committee Member

_____
Roger King, Ph.D., Committee Member

_____
Patricia Komuniecki, Ph.D., Dean
College of Graduate Studies

The University of Toledo

May 2013

An Abstract of

Design of Microwave Front-End Narrowband Filter and Limiter Components

by

Lee W. Cross

Submitted to the Graduate Faculty as partial fulfillment of the requirements for the
Doctor of Philosophy Degree in Engineering

The University of Toledo

May 2013

This dissertation proposes three novel bandpass filter structures to protect systems exposed to damaging levels of electromagnetic (EM) radiation from intentional and unintentional high-power microwave (HPM) sources. This is of interest because many commercial microwave communications and sensor systems are unprotected from high power levels. Novel technologies to harden front-end components must maintain existing system performance and cost. The proposed concepts all use low-cost printed circuit board (PCB) fabrication to create compact solutions that support high integration.

The first proposed filter achieves size reduction of 46% using a technology that is suitable for low-loss, narrowband filters that can handle high power levels. This is accomplished by reducing a substrate-integrated waveguide (SIW) loaded evanescent-mode bandpass filter to a half-mode SIW (HMSIW) structure. Demonstrated third-order SIW and HMSIW filters have 1.7 GHz center frequency and 0.2 GHz bandwidth. Simulation and measurements of the filters utilizing combline resonators prove the underlying principles.

The second proposed device combines a traditional microstrip bent hairpin filter with encapsulated gas plasma elements to create a filter-limiter: a novel narrowband filter

with integral HPM limiter behavior. An equivalent circuit model is presented for the ac-coupled plasma-shell components used in this dissertation, and parameter values were extracted from measured results and EM simulation. The theory of operation of the proposed filter-limiter was experimentally validated and key predictions were demonstrated including two modes of operation in the on state: a constant output power mode and constant attenuation mode at high power. A third-order filter-limiter with center frequency of 870 MHz was demonstrated. It operates passively from incident microwave energy, and can be primed with an external voltage source to reduce both limiter turn-on threshold power and output power variation during limiting. Limiter functionality has minimal impact on filter size, weight, performance, and cost.

The third proposed device demonstrates a large-area, light-weight plasma device that interacts with propagating X-band (8–12 GHz) microwave energy. The structure acts as a switchable EM aperture that can be integrated into a radome structure that shields enclosed antenna(s) from incident energy. Active elements are plasma-shells that are electrically excited by frequency selective surfaces (FSS) that are transparent to the frequency band of interest. The result is equivalent to large-area free-space plasma confined in a discrete layer. A novel structure was designed with the aid of full-wave simulation and was fabricated as a 76.2 mm square array. Transmission performance was tested across different drive voltages and incidence angles. Switchable attenuation of 7 dB was measured across the passband when driven with 1400 V_{pp} at 1 MHz. Plasma electron density was estimated to be 3.6×10^{12} cm^{-3} from theory and full-wave simulation. The proposed structure has potential for use on mobile platforms.

For my parents and my wife Kylie

Acknowledgements

I would like to thank Dr. Vijay Devabhaktuni and Dr. Roger King for guiding this research to a successful conclusion. I am very grateful to Dr. Mohammad Almalkawi for his expert assistance throughout this research. And most of all I am grateful to my wife for her support through all of this. I thank you all for I could not have done it without each one of you.

Table of Contents

List of Tables

List of Figures

List of Abbreviations

3-D ....three-dimensional
3G..............................third generation, uses 0.85, 0.9, 1.9, and 2.1 GHz bands
4G..............................fourth generation, uses 0.7, 0.8, 0.9, 1.8, 2.1, 2.3, & 2.6 GHz bands

ac ....alternating current
ADC ....analog to digital convertor
DAC ....digital to analog convertor
dc................................direct current
DUT ....device under test
E-beam ....electron beam
E-field ....electric field
E-plane ....waveguide symmetry plane parallel to fundamental mode E-field
EM..............................electromagnetic
EMR...........................electromagnetic radiation
FSS.............................frequency selective surface
GPS ....global positioning system, uses 1.22 and 1.57 GHz bands
H-field........................magnetic field
HFSS..........................high frequency structural simulator, a full-wave finite element
method electromagnetic simulator
HMSIW.......................half-mode substrate-integrated waveguide
HP ....Hewlett-Packard, equipment manufacturer
HPEMP ....high-power electromagnetic pulse
HPM...........................high-power microwave
IL.................................insertion loss
LNA ....low-noise amplifier
MEMS.........................microelectromechanical systems
PA ....power amplifier
PCB.............................printed circuit board
PDP ....plasma display panel
PIN ....type of diode used as a microwave switch
RF................................radio frequency
rms..............................root mean square
S-parameter ....scattering parameter
SDR.............................software defined radio
SIW ....substrate-integrated waveguide
SMT ....surface mount technology

TE..............................transverse electric
TEM ....transverse electromagnetic
TRL............................through-reflect-line, microwave calibration method
VNA...........................vector network analyzer
Wi-Fi..........................wireless networking technology based on the IEEE 802.11
standard

List of Symbols

∞ .... infinity

ε .... complex permittivity; $\varepsilon = \varepsilon_0(\varepsilon_r' + j\varepsilon_r'')$

ε_0 .... vacuum permittivity; 8.85×10^{-12} F/m

ε_r .... relative permittivity

ε_r' .... real relative permittivity

ε_r'' .... imaginary relative permittivity

λ .... wavelength

μm .... micrometer

ν .... electron collision frequency (in rad/s)

π .... pi; ~3.14

σ .... gas conductivity (in S/m)

Φ_i .... E-beam impact ionization potential (in eV)

Ω .... ohm

ω .... microwave drive frequency (in rad/s)

ω_p .... plasma frequency (in rad/s)

Ar .... argon

c .... speed of light in vacuum; 3.0×10^8 m/s

cm .... centimeter

C_n .... capacitance of nth capacitor

C_p .... parallel capacitance in plasma-shell equivalent circuit model

C_w .... wall capacitance in plasma-shell equivalent circuit model

D .... capacitive post hat diameter (in mm)

dB .... decibel

dBm .... power in decibels referenced to one milliwatt

e .... elementary charge; 1.6×10^{19} C

eV .... electron volt, unit of energy equal to 1.6×10^{-19} J

f_0 .... off state resonator resonant frequency, or filter center frequency

f_1 .... on state resonator resonant frequency

FBW .... fractional bandwidth; $(f_h - f_l)/f_0$

f_c .... critical frequency

f_{cm} .... waveguide cutoff frequency for mode m

f_h .... upper passband frequency

f_l .... lower passband frequency

$f_{\mathrm{r}m}$ ....resonator resonant frequency for mode m

g.................................unit of gram

g.................................gap length

GHz.............................gigahertz

He...............................helium

j ....imaginary unit; $\sqrt{-1}$

J_{surf}..............................surface current density (in A/m)

K.................................kelvin

k..................................two-body dissociative recombination rate constant (in cm^3/s)

kg.................................kilogram

Kr ....krypton

kV...............................kilovolt

kW..............................kilowatt

L ....length

L_n................................inductance of nth inductor

m ....meter

m_e ....electron mass; 9.1×10^{-31} kg

mg ....milligram

MHz ....megahertz

M_l...............................matching transmission line length (in mm)

mm ....millimeter

M_w..............................matching transmission line width (in mm)

N.................................gas number density (in cm^{-3})

Ne...............................neon

n_e ....electron number density (in cm^{-3})

nH...............................nanohenry

P ....power (in W)

P_i ....input power

pF ....picofarad

P_o...............................output power

Q.................................quality factor

Q_u ....unloaded quality factor

rad ....radian

R_g................................gas resistance in plasma-shell equivalent circuit model

R_n................................radius of nth post

S ....siemen

S..................................resonator spacing (in mm)

s ....second

S_{11}...............................input return loss scattering parameter

S_{21}...............................forward transmission scattering parameter

t ....thickness

$\tan(\delta)$ ....material dielectric loss tangent

t_{cu}...............................copper thickness

T_e ....electron temperature (in K)

t_{lid}.................................lid layer substrate thickness

Torr ....unit of pressure

Chapter 1

Introduction

Microwave and radio frequency (RF) technology is pervasive in modern consumer electronics. Common examples are global positioning satellite (GPS), wireless local area data networks (e.g., Wi-Fi), Bluetooth, ZigBee, third and fourth generation cellular networks (3G and 4G respectively), and radar systems. Consumer electronics are subject to relentless market forces that seek to increase capability and integration while minimizing size, weight, – and most of all – cost. Because of this pressure, most devices are left unprotected and vulnerable to damage from intentional and unintentional high-power microwave (HPM) sources. This dissertation presents novel implementations of microwave front-end components that address cost and performance concerns for consumer systems that may be exposed to high microwave power levels.

In this chapter, Section 1.1 and Section 1.2 discuss the motivation and objectives of this dissertation followed by a brief outline of each chapter in Section 1.3.

1.1 Motivation

The microwave frequency range, loosely defined as 0.3–30 GHz, is a portion of the electromagnetic (EM) spectrum commonly used for wireless communication, audio

and video broadcast, radar, power transmission, imaging, and sensors. At these frequencies, EM waves propagate through free space by line of sight and significant bandwidth is available for narrowband devices. Microwave theory is well established, and continuous advances in the areas of materials and manufacturing techniques ensure the proliferation of microwave devices for the foreseeable future. The impact of device destruction increases with growing reliance on microwave technology.

1.1.1 Threat

Microwave systems are susceptible to damage from HPM energy. While military systems are hardened against this threat, many civilian electronic systems are designed to meet only modest immunity requirements and remain unprotected. Consequently, many public and private electronic systems are vulnerable to damage from accidental exposure to high-power radars or deliberate attack by terrorists [1].

Characteristics of threat waveforms vary widely in terms of bandwidth, peak power level, average power level, rise time, and duration [2]. No single protection technology can protect against all EM threats, and practical protection devices often use several different technologies to achieve high immunity levels [3], [4]. High-power threat waveforms damage microwave components by two mechanisms. First, high-voltage transients break down insulating materials such as dielectrics, air, and packaging. Second, high-power transients cause thermal damage to conductors (e.g., bond wires and narrow traces) and small-scale semiconductor junctions. Semiconductor device vulnerability is a key issue for electronic systems because semiconductors typically have the lowest damage thresholds [5], [6].

HPM energy couples into systems through intended signal paths such as antennas and sensors, known as *front-door* coupling, and unintended entry points such as enclosure slots and wire harnesses, called *back-door* coupling. This dissertation is concerned with the former case that may be addressed by rejecting out-of-band energy (i.e., filtering) and limiting in-band energy.

For the case of front-door coupling in systems, certain parts of the RF front-end are directly exposed to high power levels. The front-end is the portion of a receiver or transmitter that operates in the RF signal frequency range. Figure 1-1 illustrates HPM front-door coupling for a direct-conversion (homodyne) transceiver architecture, a simple and flexible architecture used in many software defined radios (SDR). In this example, HPM energy propagates through free space, enters the system, and directly interacts with components highlighted in red. Energy enters through the antenna where the duplexer directs it to the receiver chain, first through the band-select filter then to the low-noise amplifier (LNA) which is the first active device and the most susceptible to damage.

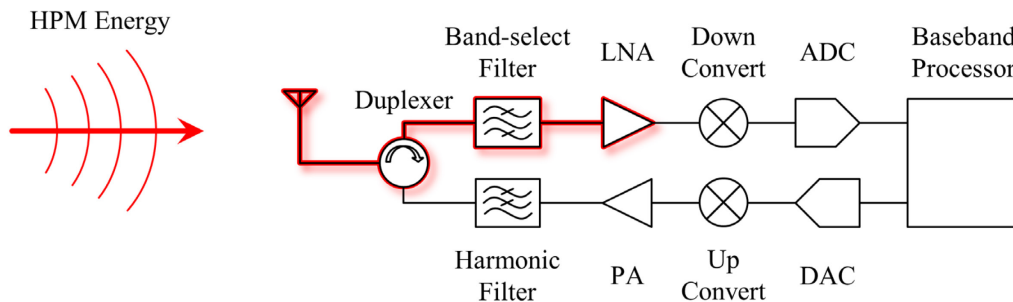Figure 1-1: Microwave direct-conversion transceiver architecture exposed to HPM energy. Components highlighted in red are directly exposed to high power.

The purpose of the band-select filter is to reject high-power signals outside the receiver band in order to prevent LNA saturation. For example, an out-of-band high-power radar would severely degrade communication performance or possibly damage the

LNA without a band-select filter. Of course, band-select filters provide no protection from high-power in-band signals. Band-select filters are specified to provide sufficient out-of-band rejection while having minimum in-band insertion loss because any insertion loss at this point in the signal chain directly subtracts from receiver sensitivity. Filter selectivity is often compromised in order to meet both requirements of adequate out-of-band rejection and acceptable insertion loss that is usually no more than 3 dB. Low-cost systems sometimes omit this filter altogether to the detriment of performance around high-power interferors.

Several approaches to hardening the previous system are presented below in Figure 1-2. The traditional approach is to add a discrete limiter device ahead of the first sensitive component which is usually the LNA. Often multiple protection stages are needed to meet protection specifications because no single technology can meet all requirements. This approach invariably increases cost and reduces performance. There are several alternative approaches to ruggedizing RF front-ends that leverage components that may already exist in the system. First, the band-select filter can reject as much out-of-band energy as possible by implementing effective narrowband filtering and should be able to handle high in-band power levels without damage. Second, it is possible to integrate low-loss limiting components into band-select filter structures, thereby merging two functions into a single filter-limiter for higher system integration and lower cost. Finally, an active frequency-selective radome can reject high-power free-space energy both out-of-band (by filtering) and in-band (by limiting) before it is received by the antenna. The HPM protection strategies of filtering out-of-band energy and limiting in-band energy will be discussed in the next two sections.
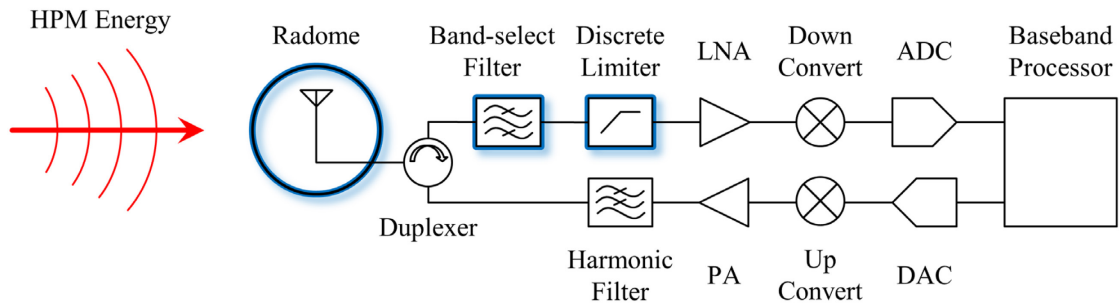
Figure 1-2: Microwave transceiver with hardening opportunities highlighted in blue. An active radome rejects HPM energy before it enters the system. A discrete limiter protects the LNA from in-band HPM energy; and the band-select filter rejects out-of-band HPM energy and can also be augmented with limiter functionality.

It should be noted that the transmitter front end may require protection as well because duplexers, often implemented as circulators, have finite port isolation and may leak energy to the power amplifier (PA). The transmitter chain can be hardened using the same principles as the receiver chain; however, the LNA remains the primary vulnerability of most systems and so the receiver chain is the focus of this dissertation.

1.1.2 Out-of-Band Filtering

The function of bandpass filters is to pass power in a certain frequency range while rejecting or attenuating power at all other frequencies. A few simple definitions are helpful in describing this behavior. Bandwidth is the width of the passband measured as the difference between the upper and lower passband frequencies f_h and f_l respectively. Passband center frequency f_0 can be approximated for narrowband filters as the average of f_h and f_l. A useful measure of relative bandwidth is fractional bandwidth (FBW) calculated as the ratio between bandwidth and center frequency. Since no absolute definitions of narrowband and wideband exist, narrowband is loosely defined as FBW less than 20%.

Narrowband filters achieve frequency selectivity by coupling EM energy to resonant structures. Stored energy within a filter is inversely related to FBW, and stored energy is directly proportional to voltage magnification (the amplification of voltage during resonance). The consequence of this is that narrowband filters can develop very high internal voltages during high-power transients and must, therefore, have mechanisms to prevent voltage breakdown [7], [8].

Filter selectivity and stopband rejection can be increased by adding sequential resonators; however, insertion loss also increases with filter order. Insertion loss is directly proportional to the unloaded quality factor (Q_u) of the resonant elements, which can be expressed as the ratio of stored energy versus loss for a resonator uncoupled to an external circuit. Narrowband filters, especially of high order, require high-Q_u resonators for acceptable insertion loss.

Microwave filters can interact with EM energy in different modes, and relevant modes for this dissertation include transverse electromagnetic (TEM) mode with microstrip structures, waveguide mode, and EM radiation (EMR) propagating through free space.

Microstrip transmission lines and resonators operating in TEM mode are very common in RF systems because they are easily implemented with printed circuit board (PCB) substrates that provide compact size, high integration, and low cost [9]. Microstrip resonator Q_u is usually in the range of 100–250, which allows implementation of many narrowband filter topologies with suitable insertion loss [10].

Waveguide structures are much larger, typically with width equal to half of one wavelength λ at low-frequency cutoff, so their use is usually restricted to high frequency

applications (i.e., above 1 GHz) [11]. Loss is far lower, leading to waveguide cavity Q_u that can be in excess of 50 000 [12]. There are many ways to reduce cavity volume while preserving Q_u superior to microstrip resonators. The method used in this dissertation is to load the waveguide cavity with capacitance so that it resonates below cutoff frequency, operating in the so-called evanescent (non-propagating) mode. Evanescent-mode operation trades volume for loss, achieving Q_u in the range of 200–2000 [13].

Waveguide cavity size can be progressively reduced using methods shown in Figure 1-3. Waveguides can be implemented in planar technology (e.g., PCB) using substrate-integrated waveguide (SIW) construction where waveguide walls are formed by copper layers and rows of vias. The substrate dielectric material loads the waveguide and reduces size. Further reduction is achieved by forming a capacitive loading post from a ring of vias and a copper "capacitive hat," creating an evanescent-mode resonator. Finally, additional reduction is achieved by cutting the SIW evanescent-mode structure in half, forming a loaded half-mode SIW (HMSIW) cavity. This will be discussed more in Section 2.1 and Chapter 3.

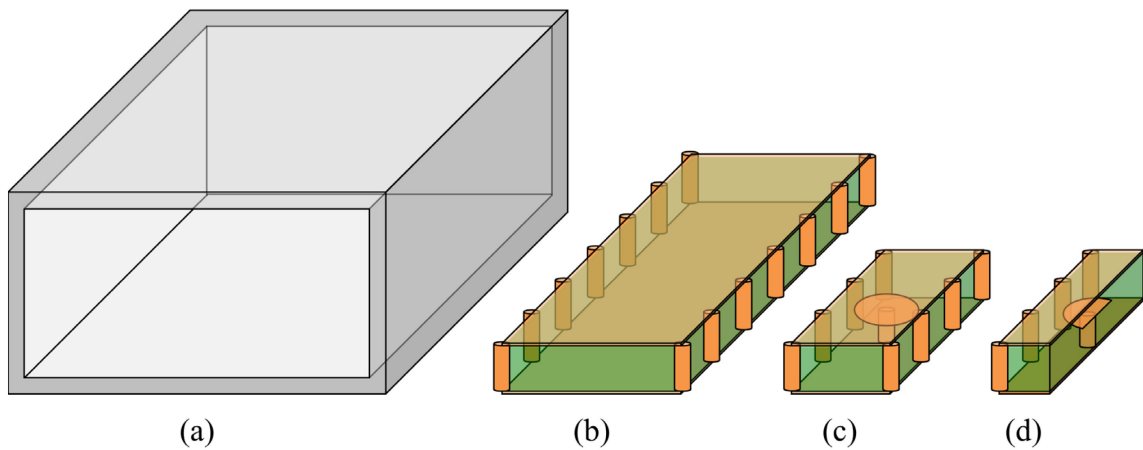(a)   (b)   (c)   (d)

Figure 1-3: (a) Unloaded waveguide cavity size is successively reduced by using (b) dielectric-loaded SIW construction, (c) adding an evanescent-mode post and capacitive hat, and (d) operating in half mode by cutting the structure in half.

Propagating EMR can also be filtered when it directly interacts with spatial filters called frequency selective surfaces (FSS) [14], [15]. Figure 1-4 shows a variety of geometric shapes commonly used as FSS elements. FSSs are used in applications including radar, communication, instrumentation, and power transfer. FSSs are used as spatial bandpass and bandstop filters, hybrid radomes, dichroic reflectors and subreflectors, absorbers, and polarizers.

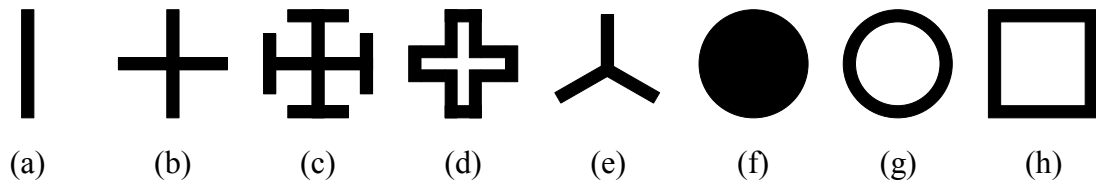(a)   (b)   (c)   (d)   (e)   (f)   (g)   (h)

Figure 1-4: Common FSS elements: (a) dipole; (b) cross dipole; (c) Jerusalem cross; (d) four-legged loaded element; (e) tripole; (f) circular; (g) ring; and (h) square loop.

Bandpass FSSs are sometimes used in radomes that protect antennas from environmental effects such as wind, rain, ice, and lightning. Radomes can also serve as a first line of defense against high-power threats by incorporating active FSS structures. A common bandpass FSS implementation that is compatible with PCB manufacturing consists of alternating layers of dielectric material and conductive planes patterned with a regular array of geometric elements. Operation is analogous to planar filters; however, performance is also affected by EMR incidence angle and polarization.

1.1.3 In-Band Limiting

Nonlinear limiter devices are used to protect sensitive devices from high power levels. The basic operating principle of microwave limiters is to act as a pass-through element with minimal loss at low incident power levels in the off state and to present a

severe impedance mismatch in the on state to reflect high power levels. Limiters can operate passively from incident power or actively from an external power source, and both operating modes will be demonstrated in this dissertation.

The nonlinear medium used in this dissertation is gas plasma. Plasma is created in low-pressure gas mixtures when electrons and ions dissociate, enabling electrons to move freely and interact with EM energy. Ion mass is orders of magnitude greater than electron mass, making ions essentially stationary at microwave frequencies and unable to significantly interact with EM energy. Plasma EM properties are, therefore, dominated by electron density, and significant microwave-plasma interaction is attainable with weakly ionized plasmas. Plasma interacts with EM energy across all frequencies, so it is useful in narrowband and wideband systems.

Plasma components used in this dissertation are referred to as plasma-shells that consist of a hollow, hermetic shell of any shape encapsulating a controlled-pressure gas that can be ionized into conductive plasma, as shown in Figure 1-5. The thin shell material is alumina, a strong and light-weight ceramic with exceptionally low loss, making plasma-shells nearly lossless components when inactive. Plasma-shells can be made at very low cost using a proprietary bulk manufacturing process.
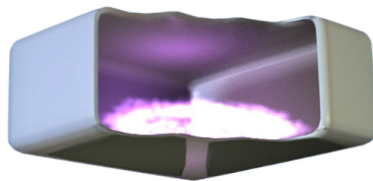

Figure 1-5: Plasma-shell cross-sectional view showing plasma across electrodes.

Conductive electrodes are patterned on one or more sides of the shell to apply an electric (E)-field of sufficient intensity to excite the interior gas into plasma. Gas

conductivity changes dramatically with the degree of plasma ionization [16] and allows the plasma-shell to be used as a switchable element.

Strongly ionized plasmas are created by high voltage and are sustained by significant power. This is the primary drawback of plasma-shells used as switchable microwave elements: they are not low-voltage, low-power elements. This restricts their usefulness to applications that can derive high voltage from incident HPM energy, or have a sufficient power budget to actively sustain plasma-shells with high voltage.

Plasma-shells operate at extreme temperatures and have long life because they are ac-coupled devices in which the electrodes are protected from direct contact with plasma by the refractory dielectric shell. This configuration eliminates electrode erosion and gas contamination unlike conventional dc-coupled plasma devices that have typical service life measured in several thousands of hours [17].

Plasma-shells are small components (i.e., typical sizes are 0.5–10 mm) that can be placed on substrates using standard surface mount technology (SMT) equipment and processes. Because of this, plasma-shells can easily be integrated into bandpass structures to limit microwave energy.

1.2 Objectives

The objective of this dissertation is to demonstrate novel hardened narrowband front-end components for systems that may be exposed to HPM energy. Effective narrowband filtering performance is required, and the addition of plasma limiter components to low-cost structures must be seamless.

The proposed components are intended to harden civilian microwave systems. Any successful technology must address key barriers to adoption including severe cost

constraints and the inability to tolerate performance degradation caused by traditional limiter technologies. Component solutions should also support high system integration and minimize size, weight, and power usage (if any). The components described in this dissertation compare favorably in all these respects.

1.3 Organization

Chapter 2 provides a literature review for the three filter/limiter structures proposed in the following chapters. The first component described in Chapter 3 is a compact, narrowband filter with center frequency of 1.7 GHz implemented as a third-order combline cavity filter with SIW construction. Dramatic size reduction of 46% is demonstrated by cutting the structure in half, and equivalent filter performance of the complete SIW and partial HMSIW filters was shown by simulation and measured results.

The following two chapters present bandpass filters with integral plasma-shell components. A combined plasma filter-limiter is proposed in Chapter 4 that consists of a microstrip bent hairpin filter structure in which each resonator has a plasma-shell mounted between the open ends, at the maximum E-field location. The first section presents ac-coupled plasma filter-limiter theory along with a simplified equivalent circuit model. The concept is experimentally demonstrated by fabricating and testing an excessively narrowband first-order filter with center frequency of 880 MHz. The device was measured in a high-power test setup across 600–900 MHz, and model parameters were extracted using measured data and EM simulations. The concept of an inexpensive plasma-shell filter-limiter was validated by fabricating and testing a practical third-order filter-limiter. Limiter performance was improved by lightly priming the plasma-shells with an external sustainer.

The final device presented in Chapter 5 is a spatial bandpass filter designed for operation at 10 GHz that uses plasma to attenuate incident energy. The second-order device is composed of PCB FSS layers that surround an array of plasma-shells that are excited by an external power supply. A small device was fabricated and tested across various incidence angles and drive voltages. Plasma parameters were estimated using plasma theory and full-wave simulation.

Chapter 6 summarizes the dissertation and discusses the significance of the work. Recommendations for further investigation are given to refine the concepts for use in practical low-cost hardened systems.

Chapter 2

Literature Review

Microwave filters are integral components in many systems, and the design and miniaturization of these filters is an ongoing research topic. Researchers seek to achieve specified performance such as bandwidth, insertion loss, and spurious-free range while minimizing size, weight, and fabrication cost. This chapter presents the state of the art for the three bandpass filter structures proposed in this dissertation. Section 2.1 presents progress in resonator cavity miniaturization using PCB substrates and describes ways that these cavities have been operated in the half mode to reduce size. Active limiter devices are introduced in Section 2.2, listing the wide variety of technologies and respective benefits and drawbacks. Some limiter elements are integrated with filter structures and examples of combined filter-limiters are discussed. Finally, Section 2.3 describes the control of propagating EMR using large-scale plasmas that have been created by various physical phenomena. The technical background for the approach used in this dissertation is presented, consisting of the integration of discrete plasma elements with spatial bandpass filter structures.

2.1 Substrate-Integrated Waveguide Miniaturization

High-performance narrowband microwave filters have traditionally been implemented in air-filled waveguide form and resulting filters are large, heavy, and costly to fabricate [11]. Waveguides can be fabricated using PCB manufacturing processes to form dielectric-loaded SIWs that reduce size, maintain waveguide performance, and are as easy to fabricate as planar microwave filters [18]. The waveguide configurations discussed in this section are shown in Figure 2-1 for reference. The SIW structure is filled with dielectric material having excellent breakdown resistance, so the structure is ideal for high-power operation [19]-[23].
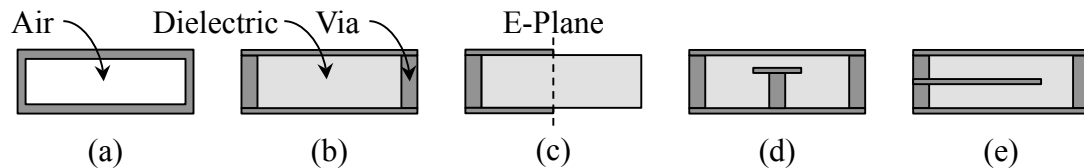

Figure 2-1: Waveguide configurations: (a) air-filled waveguide; (b) SIW; (c) half-mode SIW; (d) ridge SIW; (e) folded SIW.

Conventional SIW filters can further reduce size up to 50% by cutting the structure in half along the E-plane (feed line) axis to form the HMSIW structure [24]-[26]. Conventional HMSIW structures have low radiation loss provided they are operated above the waveguide cutoff frequency, thereby limiting usefulness in compact low-frequency microwave filters [27]. Waveguide components such as directional filters and couplers can be readily implemented with this transmission line structure [28], [29].

Loading the SIW cavity with capacitive posts allows operation below cutoff, reducing filter size and offering excellent spurious-free range that is characteristic of evanescent-mode filters [30]. Ridge SIW and folded SIW filters offer size reduction

beyond SIW and HMSIW filters when capacitively loaded to operate in the evanescent mode [31].

Evanescent-mode resonators may be fabricated within PCB substrates using many different cavity configurations and structures to achieve capacitive loading, allowing the designer considerable flexibility [32]. Substrate-integrated filters have demonstrated bandpass and bandpass-bandstop responses by coupling a series of cavities, each with a single evanescent-mode resonator per cavity [33], [34]. Reconfigurable filters and di-, tri-, and multiplexers have been made in this form [35], [36].

The concept of HMSIW resonators operating in evanescent mode has not been demonstrated in the literature and represents a significant opportunity to achieve further filter size reduction while maintaining the benefits of SIW construction.

2.2 High-Power Limiters

High-power limiters are used in RF front-ends that must survive exposure to high-power pulses. They are a standard part of all high-power pulsed radars and military microwave equipment, as well as any high-value equipment that should be protected from occasional transients, such as microwave test equipment. There are many limiter technologies that provide a variety of protection levels and benefits [37].

Diode limiters are the most common technology and are usually used as the final stage of protection. They can operate over many octaves of bandwidth [38], but impose significant insertion loss especially with multiple diode stages to handle high power levels [39], [40]. Plasma limiters provide protection up to the highest power levels, and are composed of bulky gas-filled waveguides with discharge gaps located at maximum E-field points [41]. There are also compact TEM mode transmission line plasma limiters

that employ field-enhancing features [42]. Operational life is limited in these dc-coupled structures because direct plasma contact erodes electrodes and contaminates or entraps the fill gas [43].

Several limiter technologies require support systems that are large and expensive. Multipactor limiters are useful at high power levels and have fast recovery, but require vacuum pumps and bias supplies [44], [45]. Waveguide ferrite limiters also have fast response and recovery, but are expensive, heavy, and have high insertion loss [46]. A new limiter concept uses superconducting thin films with rapidly changing electrical properties, but requires cryogenic cooling to operate [47], [48].

High integration is achieved when discrete limiter components are integrated into traditional bandpass filter structures. The combined structure is a novel HPM protection solution for cost-sensitive communication systems with narrowband filters such as RF preselect filters [49]. The filter-limiter concept was successfully demonstrated by Tan and Levy using PIN diodes in a machined combline structure [50]. This concept as presented is not suitable for low-cost civilian systems for two reasons. First, PIN diodes are damaged by high power levels and cannot tolerate high average power [51]. Second, the implemented structure is large and expensive to manufacture. These problems can be overcome by using plasma-shells as inexpensive, low-loss limiter elements mounted on a low-cost planar filter. The ac-coupled plasma-shell necessitates a new theory of operation to describe filter-limiter behavior.

2.3 Switchable Plasma Apertures

The conventional approach for creating large-area switchable EMR apertures is to combine FSSs with tunable microwave devices such as PIN diodes [52], [53], microwave

transistors [54], varactors [55], and RF MEMS [56]. One envisioned large-scale application is to selectively control RF frequency bands that enter buildings [57], and it illustrates the difficulties common to all large-area active FSSs: the need for an active device biasing scheme that doesn't degrade the frequency response and the significant cost of numerous active devices. Most applications are intended for low-power signals, and exposure to high power levels causes two critical problems. First, FSS resonant structures develop high voltage during HPM transients and must be insulated to prevent breakdown [58], [59]. Second, conventional active devices including semiconductors and RF MEMS are susceptible to damage from high power levels [60].

Operation at high power levels is possible with large-scale plasma that significantly attenuates RF communication, as seen during spacecraft vehicle reentry during which communication blackout lasts for many minutes due to the surrounding plasma sheath [61]-[63]. A plasma volume in close proximity to conductive surfaces significantly affects microwave reflection [64]-[66]. Plasma attenuates both low-power RF energy used for communication and radar tracking purposes, as well as high-power electromagnetic pulse (HPEMP) and HPM energy [67], [68].

The ability to rapidly switch large-scale plasma volumes is highly desirable for the creation of large-area EM devices with tunable operating frequency or transmission, absorption, and reflection properties. Although the concept of using plasma as a microwave absorber or reflector has existed for decades [69], [70], very few devices have been demonstrated in the literature. Such devices primarily consist of long, fragile plasma tubes. Anderson et al. presented devices using cylindrical mercury lamps as switchable plasma volumes, sharing all the problems of mercury lamps: fragility, limited life,

modulation speed limited to the kilohertz range, and toxic mercury vapor [71]. In [72], Vardaxoglou demonstrated a solid-state switchable plasma device by illuminating a patterned semiconductor wafer, but the device is likewise fragile, size limited, and very restricted in available material properties and thicknesses. Murphy et al. introduced a large-area plasma sheet reflector that operated by a pulsed electron beam and exhibited low levels of RF interaction [73]. Larigaldie and Caillault showed significant X-band (8–12 GHz) sheet reflection but only in pulsed mode with magnetic confinement [74]. Scharer et al. demonstrated RF reflection and large-volume plasma production by ultraviolet (UV) photoionization of an organic seed gas using a pulsed laser [75], [76].

None of the previously mentioned devices are suitable for large-area, rugged, rapidly switchable plasma devices. A practical solution must create and sustain plasma over a large area, use a practical power source that is compact and cost-effective, and provide controllable EM properties over the entire area. There is an opportunity to use plasma-shells as a controlled plasma environment, and FSSs as a transparent structure to deliver electrical energy to plasma within plasma-shells.

Chapter 3

Half-Mode Substrate-Integrated Waveguide Filter

This chapter presents an evanescent-mode SIW combline bandpass filter in which a cavity is loaded with capacitive posts, and then further size reduction is demonstrated by cutting the structure in half to form an HMSIW filter. This structure is a novel combination of both half-mode and evanescent-mode operation that reduces size while preserving filter performance.

The chapter is organized as follows: Sections 3.1 and 3.2 present the design and implementation of third-order filters in evanescent-mode SIW and HMSIW form. Section 3.3 presents simulation results and fabricated filter scattering (S)-parameter measurements and compares filter size with conventional SIW resonators. Section 3.4 summarizes the work and draws conclusions.

3.1 Design

The third-order bandpass filter prototype shown in Figure 3-1 is a symmetric structure in which component values and mechanical dimensions are mirrored about the center resonator, which reduces modeling and optimization effort. The topology is easily implemented in evanescent-mode SIW and HMSIW form.
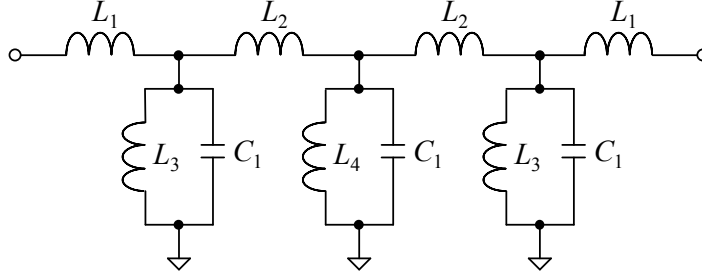
Figure 3-1: Symmetrical filter prototype with three coupled resonators and inductively coupled ports.

Resonators have identical capacitance and resonant frequency. Inter-resonator elements L_2 control bandwidth, and elements L_1 set port coupling. The design specifications are center frequency and bandwidth of 1.7 and 0.2 GHz, respectively, and return loss better than 15 dB. The ideal filter model with lumped element values in Table 3.1 achieves this specification.

Table 3.1: Ideal model values for proposed SIW and HMSIW filters.

Lumped Element	Description	SIW Value	HMSIW Value
C_1	Resonator capacitance	16.93 pF	8.47 pF
L_1	Port coupling	3.0 nH	6.2 nH
L_2	Inter-resonator coupling	6.8 nH	13.5 nH
L_3	Outer resonator inductance	0.591 nH	1.261 nH
L_4	Inner resonator inductance	0.608 nH	1.217 nH

3.1.1 Physical Structure

The prototype filter is implemented in SIW and HMSIW form as rectangular cavities loaded with three inline posts. Ports 1 and 2 are driven with 50 Ω microstrip transmission lines. High-impedance port matching lines direct-couple outer resonators with L_1. Inter-resonator magnetic coupling is realized with L_2. Resonator posts are

heavily loaded with C_1 to decrease operating frequency. SIW posts are approximated with ten-via circular arrays, and HMSIW posts are five-via semicircles.

The SIW cavity in Figure 3-2(a) consists of a ground plane defining the bottom, regularly spaced vias for sides, and a thin lid layer on top bonded to the substrate. Each post and surrounding cavity defines resonator inductors L_3 and L_4. The HMSIW filter in Figure 3-2(b) consists of the SIW cavity cut in half along the E-plane axis, exposing the centerline of the cavity and posts. Edges of the feed and matching lines are aligned with
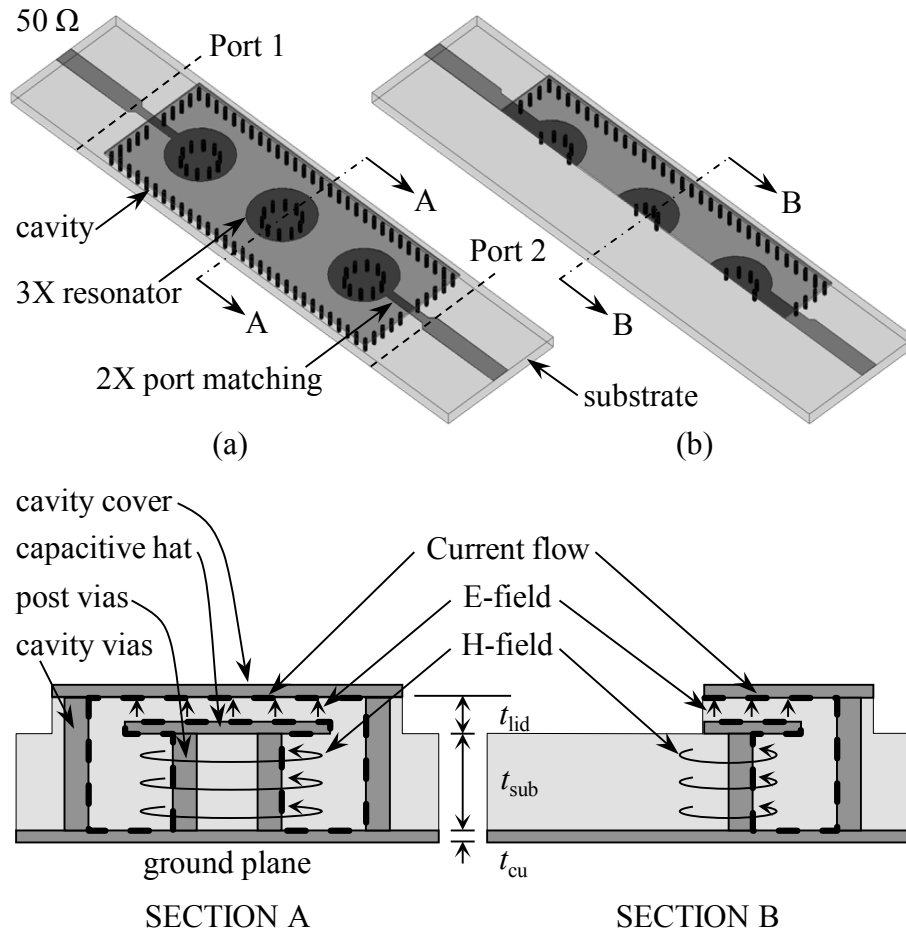

Figure 3-2: (a) SIW and (b) HMSIW filter implementations showing cavity structure, port matching lines, and resonators integrated into substrate. Sections A and B show resonator post E-field and H-field lines.

the centerline. In this way filter area is reduced by half. Parameters of the HMSIW filter were adjusted to achieve identical filter performance.

Figure 3-2 sections A and B show field lines and current flow at each resonator. Vertical vectors show E-field lines at capacitive hats and horizontal circular vectors show magnetic (H)-field lines around resonator posts. Dashed lines show the current path inside each cavity.

3.2 Implementation

The filters were designed for readily available Rogers 4003C material of base substrate layer thickness t_{sub} of 1.524 mm and lid layer thickness t_{lid} of 0.203 mm [77]. The selected lid layer material is the thinnest laminate that can be bonded to the outer layer of a PCB stackup. Relative dielectric constant ε_r used for simulation is 3.55. Dielectric loss tangent $\tan(\delta)$ is 0.0021, which sets an upper limit for resonator Q_u. Copper thickness t_{cu} is 35 μm (1 oz weight). Microstrip width of 3.35 mm achieves 50 Ω impedance. Filter models were optimized and simulated in ANSYS HFSS [78].

Filter geometry was optimized to achieve specified performance with as many similar measurements as possible to facilitate area comparison. Cavity width was set to 20 and 10 mm for SIW and HMSIW filters respectively. Dimensions shown in Figure 3-3 and Table 3.2 achieve identical filter response and similar cavity length L. The HMSIW filter requires smaller post radii R_1 and R_2 to maintain equal center frequency. Weaker port and inter-resonator coupling are realized with higher impedance matching lines (reduced M_w) and longer inter-resonator spacing S.
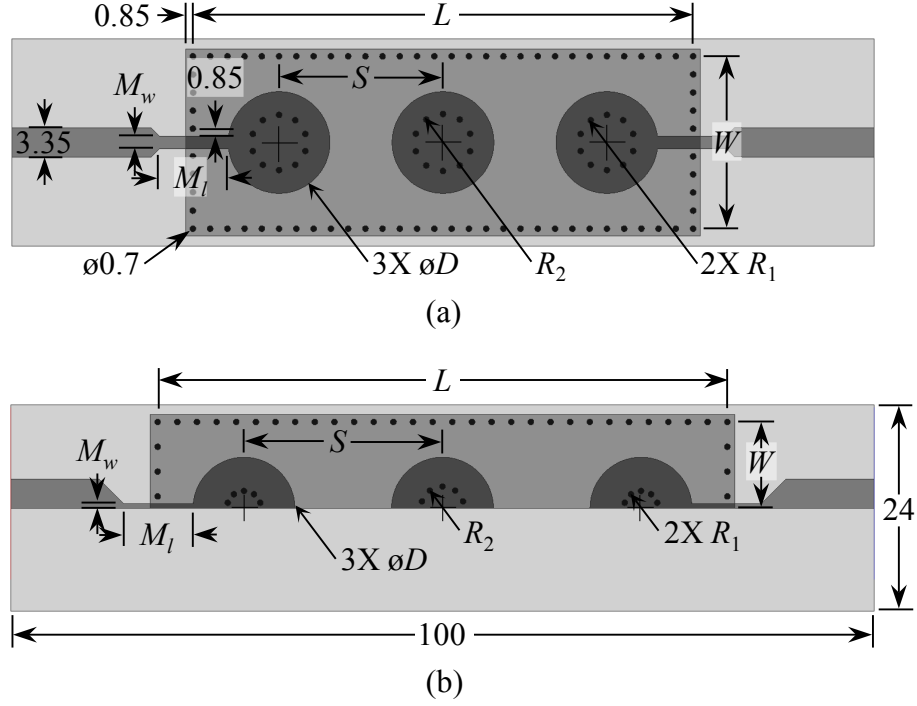
Figure 3-3: Physical dimensions of (a) SIW; and (b) HMSIW filters. (All units in mm)

Table 3.2: Dimensions of proposed SIW and HMSIW filters.

Lumped Element	Description	SIW Value (mm)	HMSIW Value (mm)
L	Cavity length	57.20	62.20
W	Cavity width	20.00	10.00
S	Resonator spacing	18.60	21.10
R_1	Outer post radius	2.82	1.98
R_2	Inner post radius	2.90	2.50
M_w	Matching line width	2.50	0.50
M_l	Matching line length	8.00	8.00
D	Post hat diameter	11.80	11.80
t_{lid}	Lid layer thickness	0.203	0.203
t_{sub}	Substrate thickness	1.524	1.524
t_{cu}	Copper thickness	0.035	0.035

Capacitive hats are fixed diameter D and C_1 is calculated from

$$C_1 = \frac{\varepsilon_0 \varepsilon_r \pi (D/2)^2}{t_{lid}}$$

(3.1)

23

to be 16.93 pF for SIW and 8.47 pF for HMSIW posts neglecting fringing capacitance. Resonator inductance is the equivalent inductance of a shorted coaxial transmission line with center profile of the circular via array and outer profile of the cavity [79]. Characteristic impedance of the irregular shape need not be directly computed; the post via array radius is simply adjusted to tune each resonator. Passband center frequency is determined by hat capacitance in conjunction with resonator inductance and is set to 1.7 GHz by selecting appropriate values for D and t_{sub} respectively.

Filter substrates in Figure 3-4 were fabricated using standard two-layer PCB processing and impedance control for ±10% transmission line tolerance. Lid layers were fabricated from single-sided laminate and attached to substrates with short wires soldered through each via barrel connecting top and bottom.

3.3 Results and Discussion

The proposed filters were measured with a Rohde & Schwarz ZVB20 vector network analyzer (VNA) with through-reflect-line (TRL) calibration. The air gap between lid layer and substrate layer was minimized with pressure at each resonator post.

Measured transmission (S_{21}) and return loss (S_{11}) S-parameter responses are shown in Figure 3-5. Both fabricated filters demonstrate nearly identical bandwidth, center frequency, and insertion loss. The inconsistent air gap resulted in a slightly higher passband center frequency as expected. Average insertion loss is 0.9 and 1.1 dB for the SIW and HMSIW filters respectively, which implies similar resonator Q_u between the two designs. Measured results show excellent agreement with simulations.

Surface current density is shown in Figure 3-6 for both filters. Current on the cavity top is not shown and the lid and substrate are transparent to see within the cavity
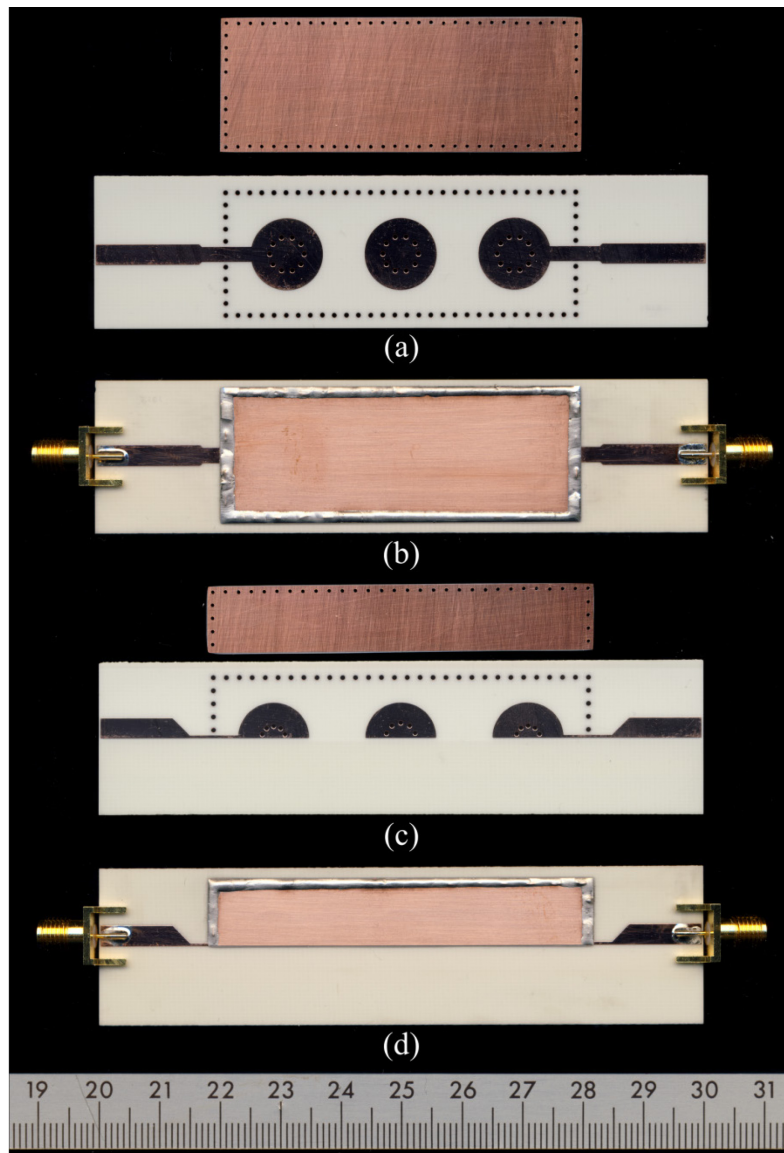
Figure 3-4: Photographs of the evanescent-mode SIW and HMSIW filters: (a) SIW lid and substrate layers before assembly; (b) assembled SIW filter; (c) HMSIW lid and substrate layers before assembly; and (d) assembled HMSIW filter.

structure. The SIW filter in Figure 3-6(a) is sectioned along the center of the feed line to show current crowding at the base of the posts, which is also evident in the HMSIW filter in Figure 3-6(b). Current is effectively contained within the cavity walls, although the HMSIW cavity opening allows some current outside the cavity.
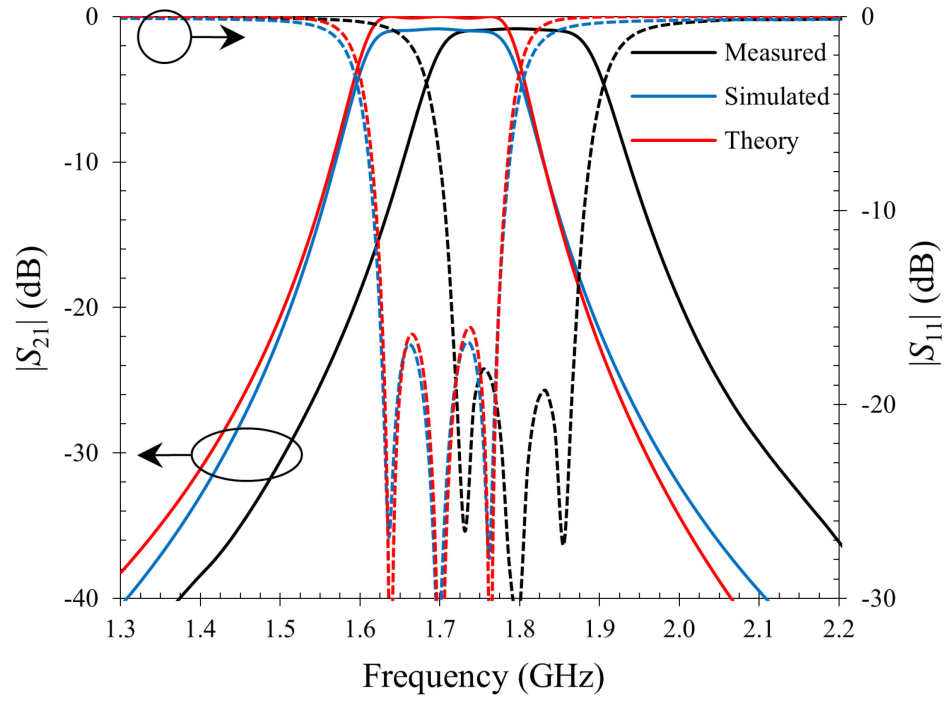
(a)
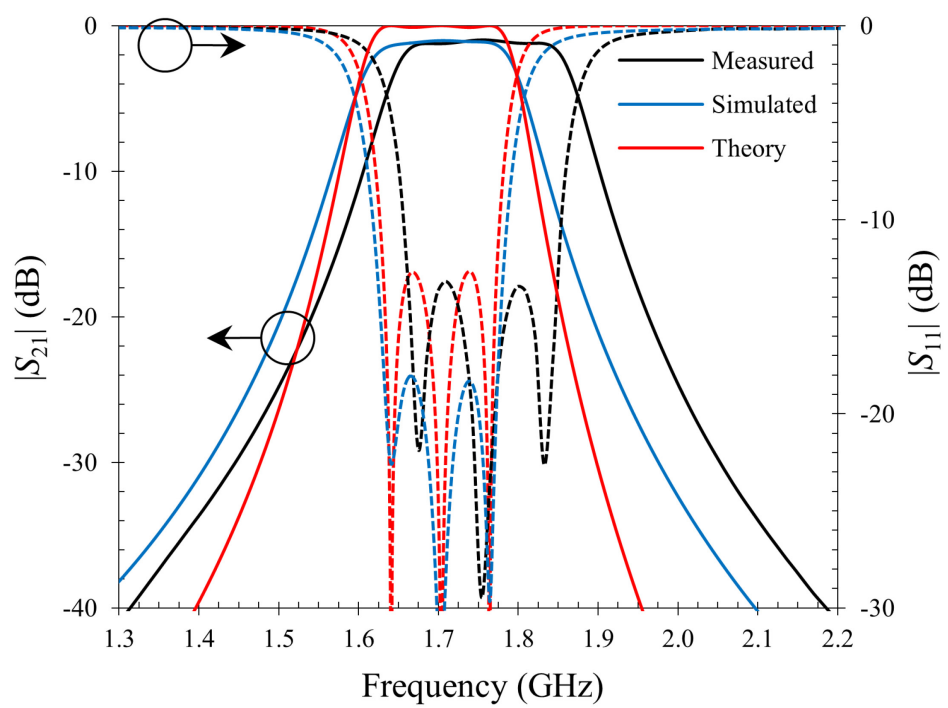
(b)

Figure 3-5: Measured, simulated, and theory results of passband S-parameters for (a) proposed SIW; and (b) HMSIW filters.
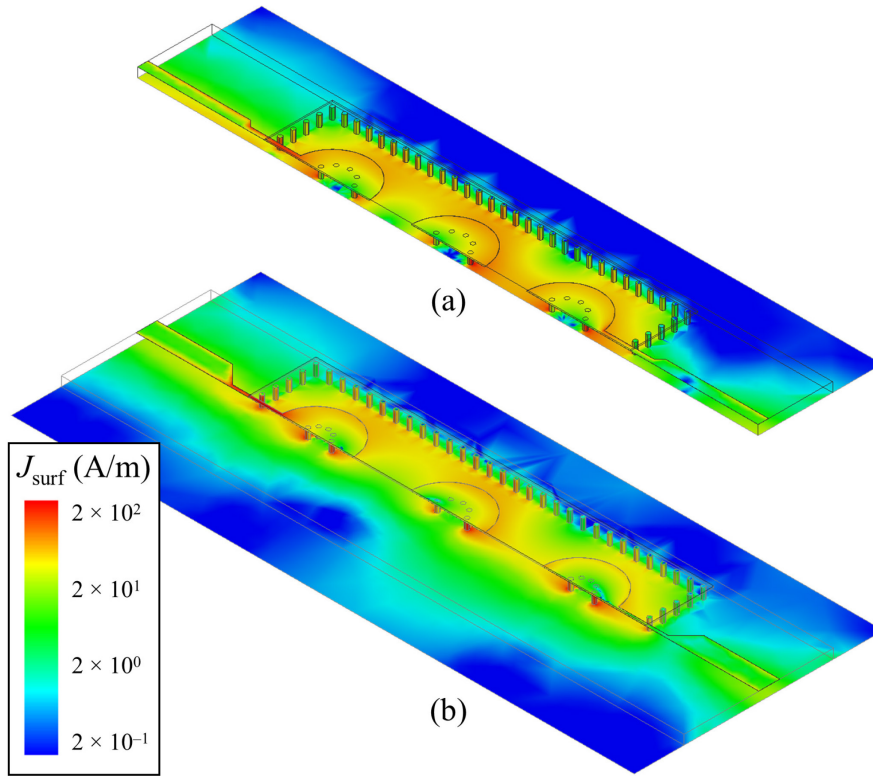
Figure 3-6: Surface current density at 1.7 GHz for proposed (a) sectioned SIW; and (b) full HMSIW filters shows current confinement within cavities and current crowding at resonator posts.

The wideband responses in Figure 3-7 show spurious-free performance to at least 6.5 GHz for the SIW filter and beyond 8 GHz for the HMSIW filter. The spurious-free range can be increased further by reducing the substrate dielectric constant or reducing capacitive hat diameter, both of which increase the filter resonant frequency and must be compensated by increasing cavity size or decreasing post radius.

A concern of cutting the cavity in half is radiating energy from the open structure. The broadband filter responses show similar SIW and HMSIW performance, particularly with nearly identical S_{21} traces up to the spurious response frequency range; this means significant energy is not radiated from the cavity relative to the SIW structure. Unlike a
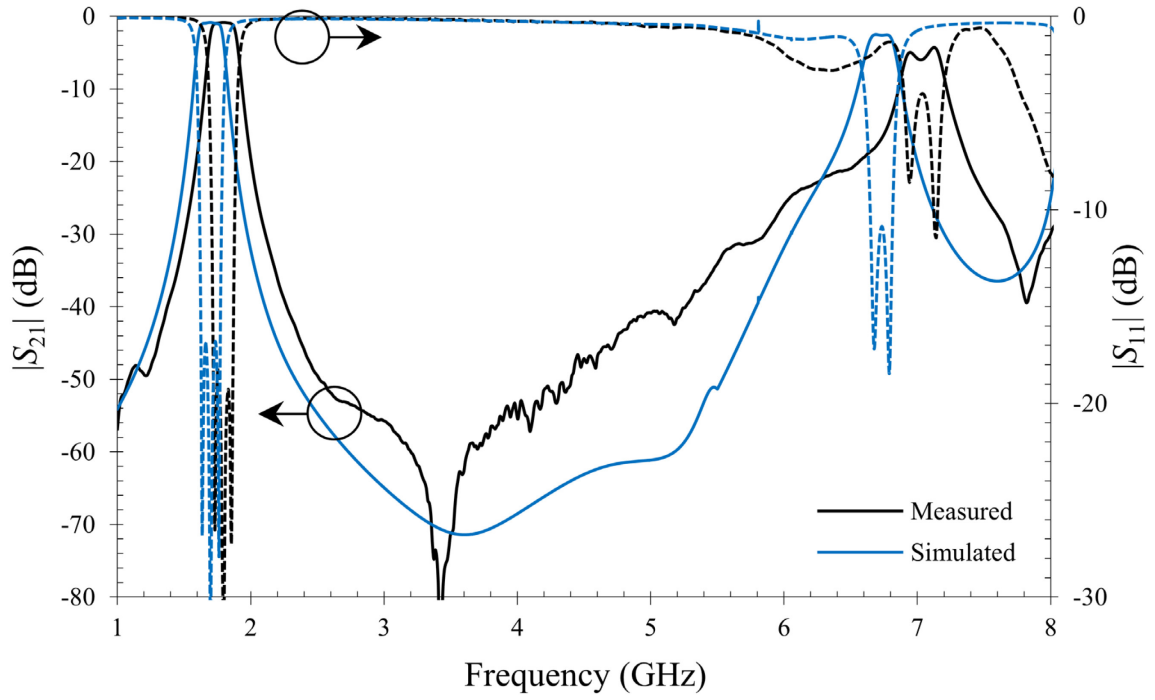
(a)
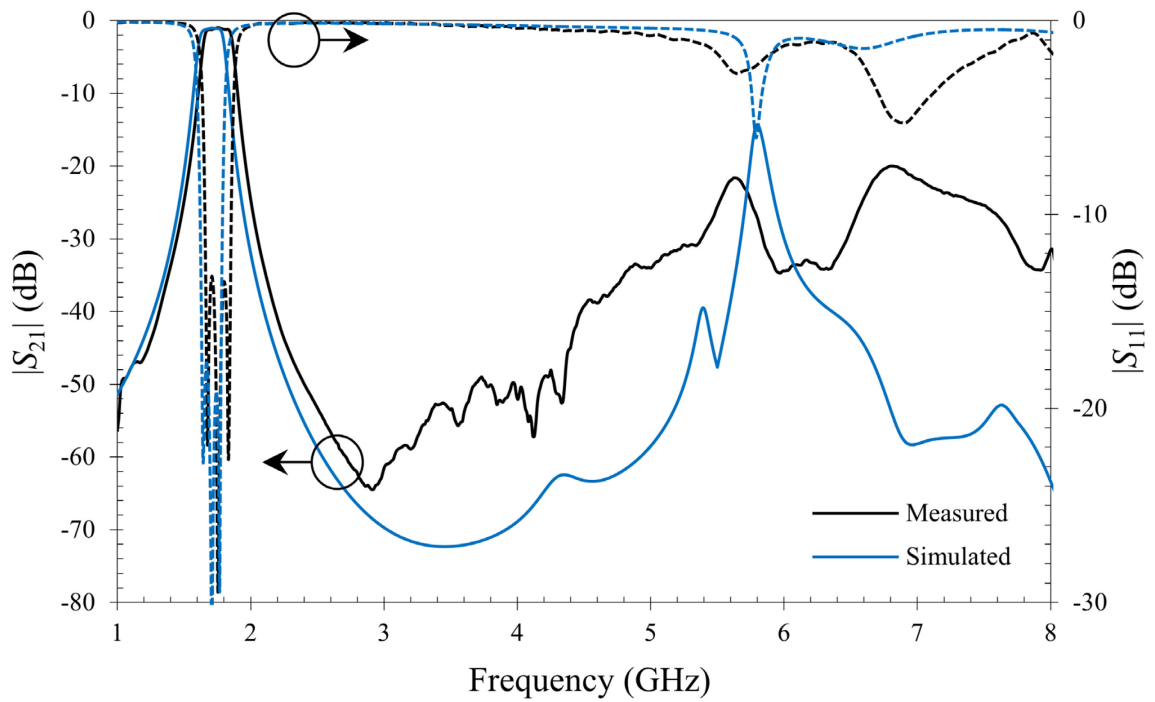
(b)

Figure 3-7: Measured and simulated broadband filter response for proposed (a) SIW; and (b) HMSIW filters showing spurious-free response to at least 6.5 GHz for the SIW filter and beyond 8 GHz for the HMSIW filter.

conventional HMSIW filter, energy is well-contained by the evanescent-mode cavity structure in which the passband center frequency is half the cavity cutoff frequency.

3.3.1 Comparison to Conventional SIW Filter

Conventional waveguide filters, whether using air-filled metallic waveguide or dielectric-filled SIW resonators, have resonator area bounded by equations from [80]. Resonator width W is calculated from (3.2) where cutoff frequency f_{c10} is set below the filter passband for the dominant TE_{10} mode of a waveguide filled with material of relative dielectric constant ε_r, and c is the speed of light in vacuum.

$$f_{c10} = \frac{c}{2W\sqrt{\varepsilon_r}} \tag{3.2}$$

Resonator length L is solved from (3.3) where the resonator resonant frequency f_{r101} is set equal to the filter center frequency.

$$f_{r101} = \frac{c}{2\sqrt{\varepsilon_r}}\sqrt{(1/W)^2 + (1/L)^2} \tag{3.3}$$

For a conventional waveguide filter with center frequency of 1.7 GHz fabricated from the same material as the proposed filters, each resonator can be 66 mm × 66 mm for minimum possible third-order filter area of 131 cm^2. The first spurious passband f_{r102} is calculated from (3.4) to be 2.7 GHz, which is much closer to the passband than with evanescent-mode SIW and HMSIW filters.

$$f_{r102} = \frac{c}{2\sqrt{\varepsilon_r}}\sqrt{(1/W)^2 + (2/L)^2} \tag{3.4}$$

Air-filled waveguide is much larger with resonators of 125 mm × 125 mm for minimum possible filter area of 467 cm^2, and the first spurious passband is the same as before. This shows that size reduction of evanescent-mode filters is significant versus waveguide filter implementation. Comparing the examples presented in this section, the SIW evanescent-mode filter area is 11.4 cm^2 versus the conventional SIW filter area of 131 cm^2. The HMSIW filter is even smaller with area of only 6.2 cm^2, for a size reduction of 46% with similar performance.

3.4 Conclusions

This chapter introduced a novel evanescent-mode HMSIW bandpass filter. For comparison purposes, two filters (SIW and HMSIW) were designed for center frequency of 1.7 GHz and bandwidth of 0.2 GHz. The proposed HMSIW filter demonstrates size reduction of 46% versus a similar SIW filter, with equivalent performance in terms of insertion loss and first spurious response frequency. Filter size reduction is dramatic when compared to conventional SIW filter implementations. Evanescent-mode SIW and HMSIW resonator Q_u is equivalent as evidenced by similar insertion loss.

The demonstrated size reduction is important for reducing filter volume, cost, and weight. Large-area arrays such as filter banks and multiplexers will benefit greatly from this novel structure. The HMSIW structure is suitable for exposure to HPM transients because it is fully insulated by the substrate material. It is believed that this type of filter will find wide usage in advanced RF/microwave transceiver front-ends.

Chapter 4

Microstrip Plasma Filter-Limiter

High system integration can be achieved by integrating a bandpass filter with nonlinear limiter elements. The proposed concept is derived from a microstrip bent hairpin filter, shown in Figure 4-1(a), which is known for compact size and low-cost fabrication with excellent electrical performance [81], [82]. Plasma-shells are placed across the ends of each $\lambda/2$ resonator as shown in Figure 4-1(b) where there is high E-field gradient at resonance. The combined filter-limiter acts as a bandpass filter in the off state (i.e., without plasma) and as a high-power limiter in the on state (i.e., with plasma). It is worth mentioning that this series-connected configuration provides twice the voltage
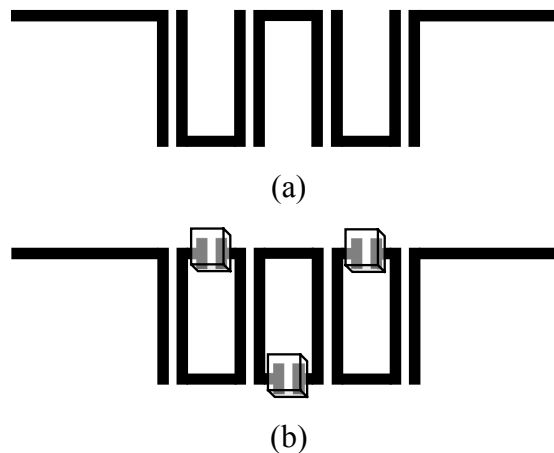

(a)

(b)

Figure 4-1: (a) Traditional microstrip bent hairpin filter; and (b) proposed plasma filter-limiter with plasma-shells placed at maximum E-field locations.

across plasma-shells versus a grounded $\lambda/4$ resonator with shunt-connected plasma-shells, and higher voltage reduces turn-on threshold power and activation time. For optimal limiter design, voltage across plasma-shells should be maximized by increasing resonator characteristic impedance, which must be balanced with decreasing Q-factor.

Although the resonator structure looks similar to the square open loop resonator, it is more closely related to the bent hairpin filter because the primary design motivations are area reduction and maximized E-field, rather than readily accomplished cross-coupled filter topologies [83], [84]. Cross-coupling with plasma limiter elements would cause an undesirable behavior – each transmission zero would create a spurious passband at high incident power levels, which may be more appropriate for a high-power multiplexer or Q-switch.

Gas plasma devices using low-pressure noble gas mixtures often exhibit relatively low conductivity, although there is much room for improvement through optimization of many variables including gas mixture, gas pressure, drive waveform, electrode geometry, wall material, and priming methods [85]. However, optimization is beyond the scope of this dissertation. Even with low on-state conductivity, placing the plasma element in a resonant structure allows voltage magnification to effectively transform gas conductivity to a much higher value capable of considerable impedance mismatch during limiting. In the off state, the plasma-shell has the potential for near-zero loss, minimizing impact on filter performance.

This chapter is organized as follows: Section 4.1 presents ac-coupled plasma filter-limiter theory and validates it with a single resonator fixture. Section 4.2 describes the design, modeling, and measurement of a third-order filter-limiter showing good

agreement in both the off and on states. Section 4.3 summarizes the work and draws conclusions.

4.1 Theory

4.1.1 Plasma Element

The basic operating principle of a plasma limiter is that when forward power exceeds turn-on threshold power, a plasma discharge creates a low-impedance discontinuity that initiates on the time scale of hundreds of picoseconds to hundreds of nanoseconds. In the on state, the plasma operates in a constant-voltage regime and limits forward power to a "clamping" value, absorbing and reflecting the remaining power. Plasma exists until forward power falls below the turn-off threshold, decaying to the off state with a recombination time constant on the order of microseconds [86], [87].

Electrodes are the electrical interface between the internal plasma and external circuit. Plasma-shells can be electroded in any geometry across multiple sides. Plasma-shells used in this device are electroded on one side with a 0.5 mm gap. Overall dimensions are 4.6 mm × 4.6 mm × 2.0 mm with 300 μm wall thickness, weighing 71 mg each. Fill gas is 0.1% argon with balance of neon, a common Penning mixture [88], at 240 Torr. Figure 4-2 shows how plasma-shells are placed on PCB substrates using standard SMT processes.

4.1.2 Plasma-Shell Equivalent Circuit

The plasma-shell equivalent circuit model shown in Figure 4-3 is adapted from Slottow and Bitzer's classic ac-coupled two-electrode plasma display panel (PDP) pixel
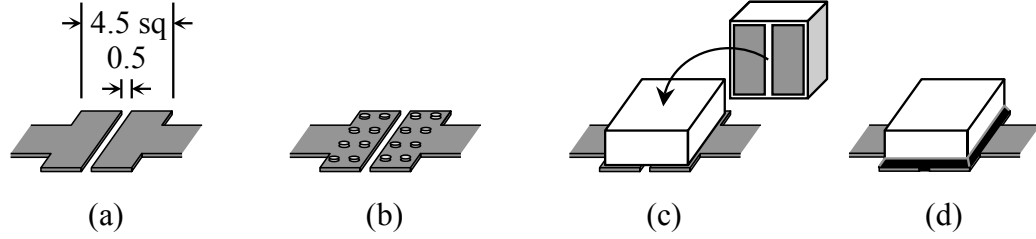
Figure 4-2: Plasma-shell SMT assembly process in which (a) the PCB pad is (b) stenciled with conductive epoxy then (c) the shell is machine placed and (d) the high E-field gap and electrodes are sealed with underfill epoxy. (All units in mm)
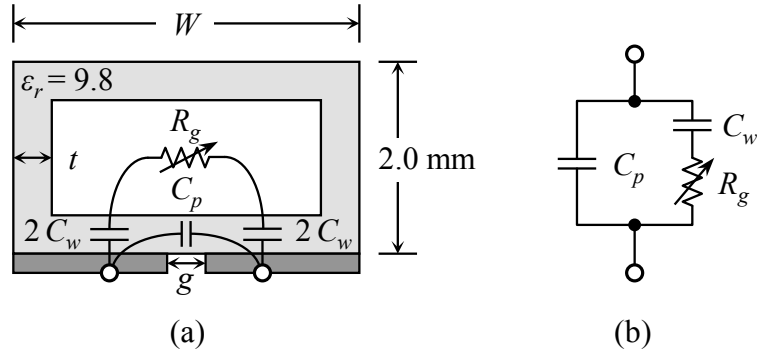

Figure 4-3: Electroded plasma-shell (a) physical structure and (b) simplified equivalent circuit model.

equivalent circuit model [89], in which electrodes apply E-field across the enclosed gas through a thin dielectric layer (i.e., the shell wall). Wall capacitance C_w is in series with gas impedance R_g, and a small parallel capacitance C_p accounts for the high-dielectric-constant shell in contact with electrodes. The off-state model simplifies to C_p, and the on-state model includes parallel impedance from gas that ionizes into a plasma sheet (R_g) in series with C_w. This simple model is sufficient to predict first-order effects caused by changes in gas conductivity. Equation (4.1) estimates the upper-bound of C_w as half the capacitance of one electrode across the shell and evaluates to

$$C_w \leq \frac{1}{2}\varepsilon_0\varepsilon_r \frac{(W-2t)\times(W-2t-g)/2}{t} = 1.1\,\text{pF}. \tag{4.1}$$

4.1.3 First-Order Validation

Theoretical performance of a first-order filter-limiter is shown in Figure 4-4. In the off state, the filter exhibits center frequency f_0. Insertion loss increases to nearly the maximum value as the gas ionizes and R_g approaches the critical value equal to the shell wall reactance at the critical frequency f_c. With $R_g > 1/(\omega C_w)$, the plasma-shell acts as a lossy element that dominates the response with high insertion loss. With $R_g < 1/(\omega C_w)$, wall capacitance C_w dominates the response and a spurious passband emerges at $f_1 \ll f_0$. This is not as problematic as it appears for several reasons: emergence of the spurious passband requires very high power levels and is well outside the filter passband, and subsequent filter-limiter stages will attenuate the spurious passband.
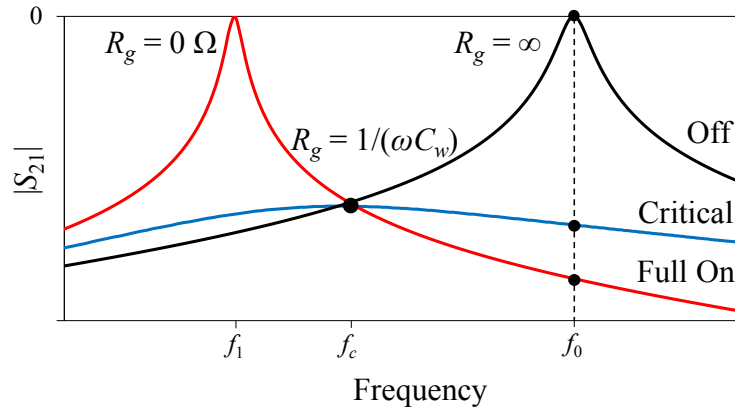

Figure 4-4: First-order filter-limiter theoretical operation in off, critical, and on states shows high attenuation at critical gas conductivity and emergence of a spurious passband at high gas conductivity.

The filter-limiter shown in Figure 4-5 was built to validate the proposed plasma-shell circuit model in its application as a filter-limiter. The design specifications are $f_0 = 880$ MHz to coincide with the center frequency of the test system amplifier power band, and narrow bandwidth of 1% for maximum voltage across the plasma-shell. Resonator

trace width was chosen to be 2.5 mm as a tradeoff between higher characteristic impedance (Z_0) of 60 Ω and sufficient Q_u. Port coupling is adjusted by the spacing between the magnetically coupled feed lines and resonator [90]. Filters in this chapter were photo-etched from Rogers 4003C with 18 μm copper-clad.
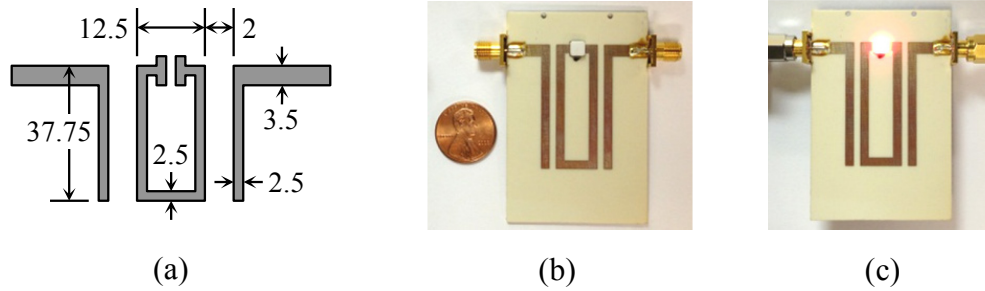

<center>(a)   (b)   (c)</center>

Figure 4-5: First-order filter-limiter (a) layout and (b) fabricated device in off state and (c) on state. (All units in mm)

Filter *S*-parameters were measured with an HP 8720B VNA first without a plasma-shell, and the measured passband was f_0 = 987 MHz with FBW of 1.3% and insertion loss of 3.0 dB. Mounting the plasma-shell reduced the passband to f_0 = 867 MHz with FBW of 1.2% and insertion loss of 4.7 dB.

Filter geometry was modeled with the aid of Sonnet EM which is based on the method of moments [91]. A lumped port was defined at the plasma-shell pad to model plasma-shell terminal impedance (Z_p) as an *S*-parameter component, allowing estimates of model parameters and filter performance. Figure 4-6 shows good agreement between: measured results, the Sonnet model with substrate parameters set to ε_r = 3.95 and tan(δ) = 0.0021, and the lossless circuit theory model in Figure 4-7 optimized to match measured data.

Plasma-shell model values were determined by adjusting Sonnet model parameters to match measured results. First, C_p was determined to be 0.33 pF by
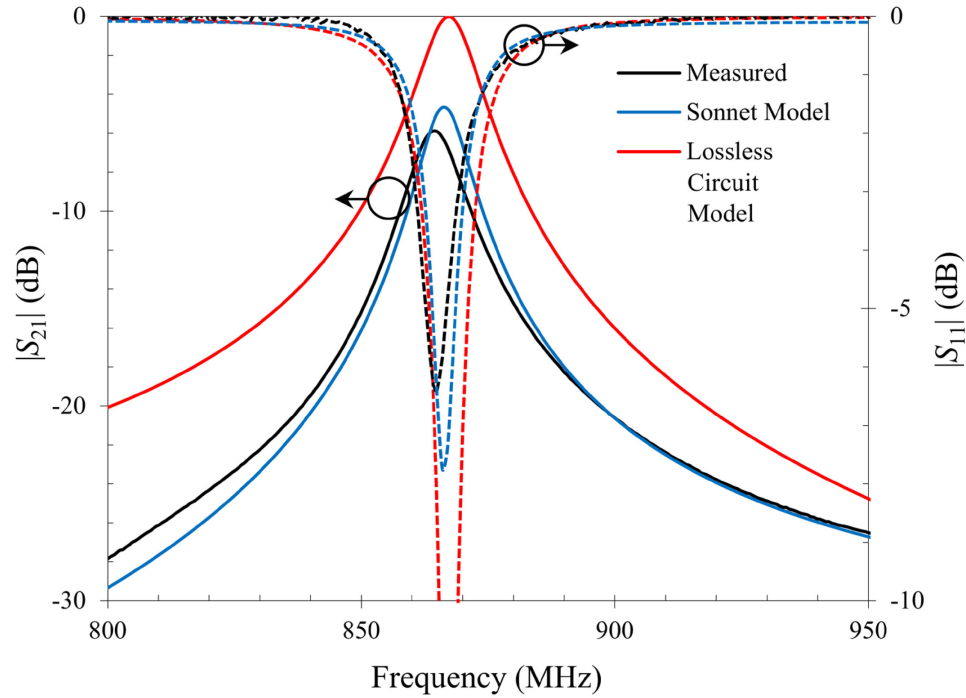
<center>36</center>

Figure 4-6: First-order filter-limiter measured results compared to the Sonnet model and lossless circuit model.
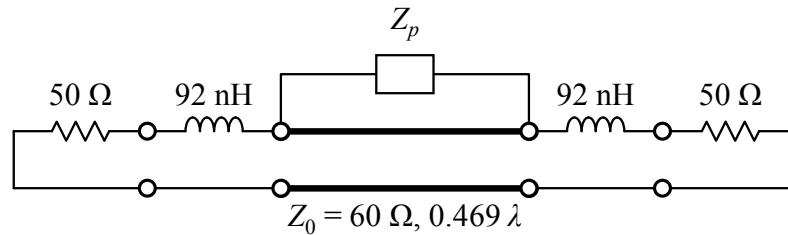

Figure 4-7: First-order filter-limiter lossless distributed circuit model.

adjusting capacitance so that f_0 reduces from 987 MHz (with $C_p = 0$ pF) to 867 MHz. This uses S-parameter measurements in the off state, and the remaining parameters were extracted from filter-limiter measured data in the on state.

The on-state wideband response is difficult to measure because of high power levels. The test setup in Figure 4-8 isolates sensitive measurement equipment from high-power pulses. It consists of a modulated pulse source that outputs up to 54 dBm over a useful range of 820–920 MHz and two different measurement configurations.

Figure 4-8(b) is a high-dynamic-range setup that allows attenuation measurement of the device under test (DUT) at frequencies other than the drive frequency. The HP 8566B spectrum analyzer has dynamic range of 125 dB (much greater than the VNA), which is necessary to measure the 15 dBm measurement signal through the 35 dB directional coupler and 20 dB attenuator, providing measurement dynamic range of 70 dB. Measurement setup frequency response is flat over 600–900 MHz. A drive pulse repetition rate of 10 pulses per second with 12.5% duty cycle reduces thermal effects at high power levels. Figure 4-8(c) is a traditional limiter measurement setup that measures input and output power across the DUT with an HP 438A power meter and HP 8481A sensors.
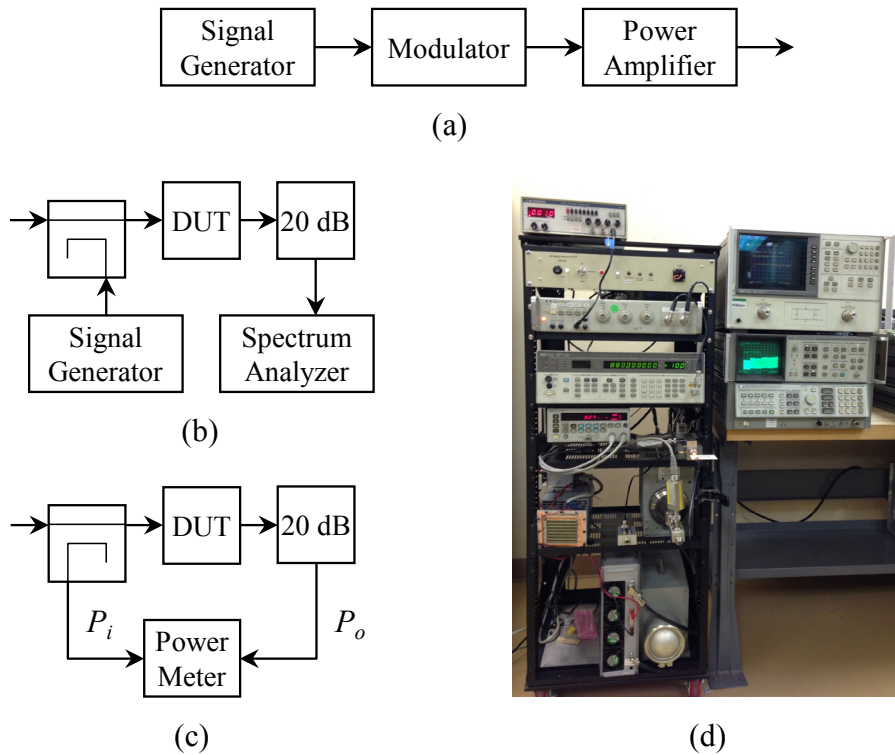

Figure 4-8: High-power test setup consisting of (a) modulated power source; (b) high-dynamic-range wideband test setup; (c) limiter attenuation test setup; and (d) picture of the equipment.

Wideband measured results are shown in Figure 4-9 as discrete data points taken at regular frequency intervals and input power increasing in decades. The next model parameter to extract is C_w, which could be directly measured from the spurious passband frequency when $R_g = 0\ \Omega$, but such high gas conductivity cannot be achieved with this setup. A realistic approach is to extract C_w from the critical point where transmission responses cross for all input power levels, located at $f_c = 775$ MHz. C_w was determined to be 0.73 pF by setting $R_g = 0\ \Omega$ in the Sonnet model and adjusting C_w until the response intersected the critical point. The extracted value is less than predicted by (4.1) likely because the plasma sheet is weakly ionized far from the electrode gap, reducing its effective area.
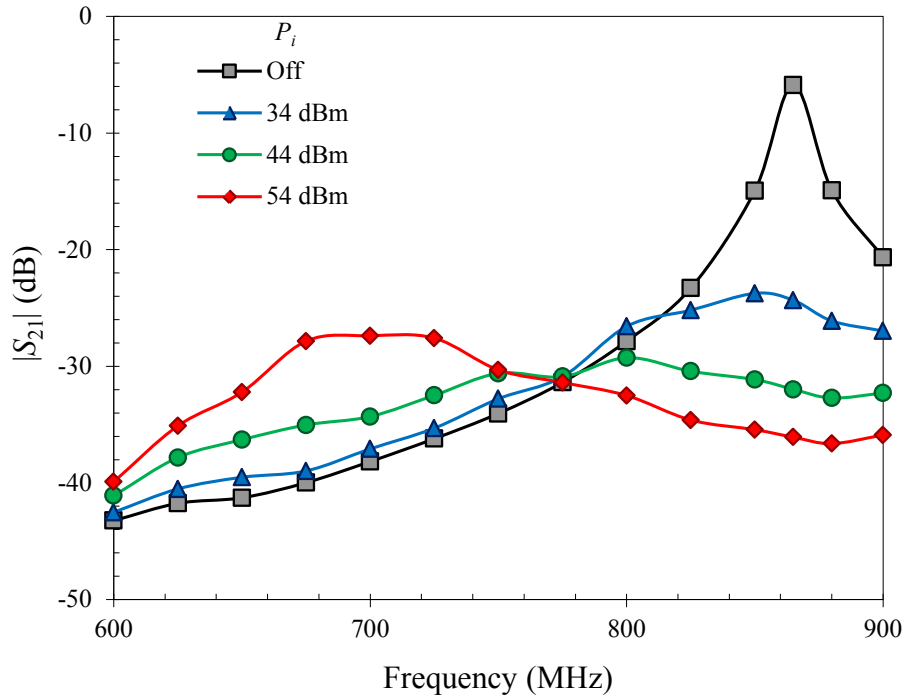

Figure 4-9: First-order filter-limiter wideband results show passband disappearance at f_0 with increasing input power, and spurious passband emergence at the highest tested power level. All traces cross at the critical point at 775 MHz.

Finally, R_g was estimated by optimizing Sonnet model values to match measured wideband test data at each input power level. Values of R_g are given in Figure 4-10 for each tested power level in Figure 4-9. It is observed that the wideband response with input power of 44 dBm matches the Sonnet EM model with R_g equal to the critical gas resistance of 280 Ω, showing a nearly flat response with peak at the critical point. The Sonnet model predicts the location of the spurious passband to be f_1 = 698 MHz (with R_g = 0 Ω).
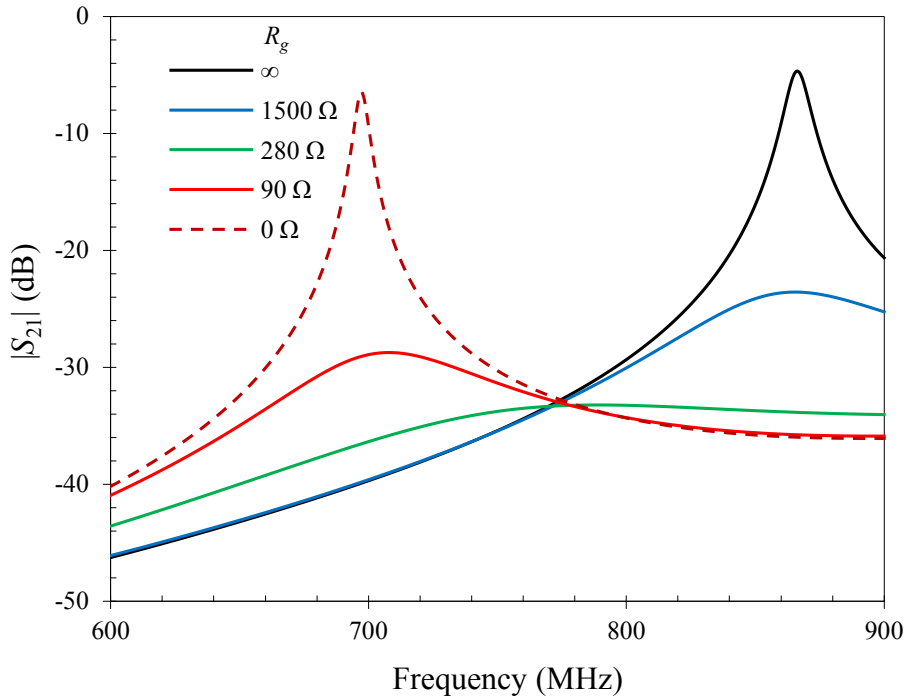
Figure 4-10: Sonnet model results agree with measured results in Figure 4-9 with optimized R_g values (given in the legend) for each tested input power level. The Sonnet model predicts a spurious passband at 698 MHz for R_g = 0 Ω.

With accurate model parameters extracted, the test setup in Figure 4-8(c) was used to measure input and output power with high-power pulses at drive frequency f_0 = 867 MHz. The off-state trace in Figure 4-11 shows power passing directly through the filter less insertion loss with slope of 1, and the plasma-shell self-activates at turn-on

threshold power of 28 dBm. While in the on state at low incident power, output power is clamped to ~8 dBm with slope of 0.14. Flat slope defines the limiter region where the plasma-shell acts as a constant-voltage limiter where gas conductivity modulates to hold output power constant independent of input power. The plasma-shell remains on until input power falls below 14 dBm, showing a hysteresis region of 14 dB.
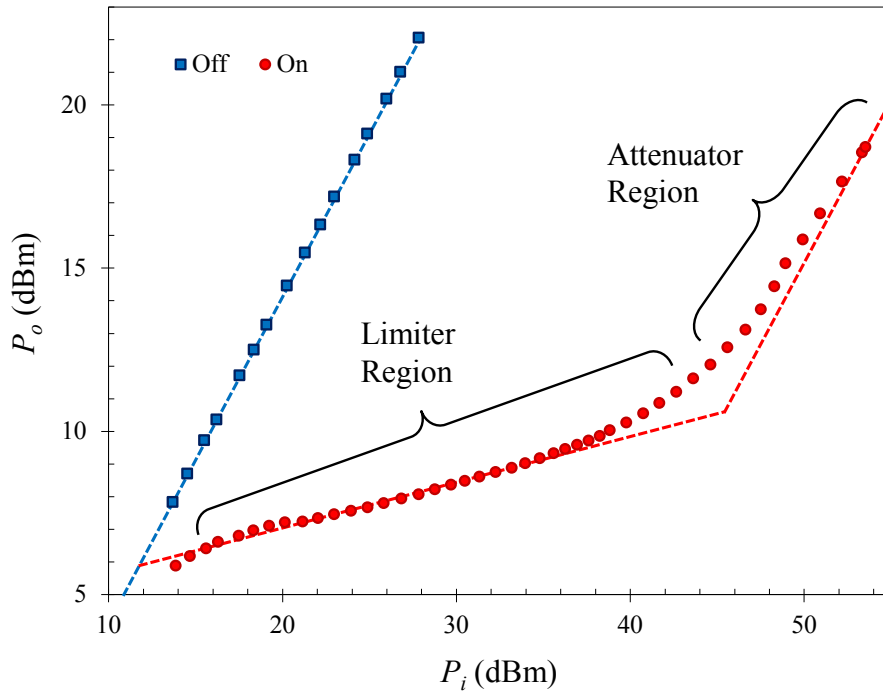
Figure 4-11: First-order filter-limiter characteristic curve in the off and on states showing distinct limiter and attenuator operating regions.

Voltage across plasma-shell terminals cannot be directly measured but can be predicted by the Sonnet model. The voltage multiplication factor is determined to be 16.8 by applying a known forward power and measuring voltage across the plasma-shell terminals. Plasma-shell turn-on threshold voltage is 133 V, calculated as the product of the filter input voltage at turn-on threshold power, voltage multiplication factor, and $\sqrt{2}$ to convert rms to peak voltage.

At input power levels above 46 dBm, the device operates in the attenuator region where slope is 1 and the device has high fixed insertion loss independent of input power. Measurements show slope approaching 1 at the highest tested power level. Measured attenuation at 46 dBm is 33.5 dB, similar to the value of 29.1 dB predicted by the Sonnet model with critical gas conductivity ($R_g = 280\ \Omega$). Higher attenuation can be achieved by cascading filter-limiter stages.

4.2 Third-Order Filter-Limiter

With plasma-shell model parameters extracted and theory validated, a filter-limiter of higher order was designed to confirm the validity of the proposed concept and to demonstrate higher attenuation in a practical structure. The third-order bandpass filter specifications are $f_0 = 880$ MHz and FBW of 5%. The fabricated filter is shown with dimensions in Figure 4-12. With plasma-shells mounted, the off-state measured response is shown in Figure 4-13 with $f_0 = 872$ MHz, FBW of 4.9%, and insertion loss of 3.3 dB. Off-state measured results match the Sonnet model and lossless circuit model in Figure 4-14.

The wideband transmission response is shown in Figure 4-15, driven near the passband center at 870 MHz with increasing power levels. The passband disappears as

(a)   (b)
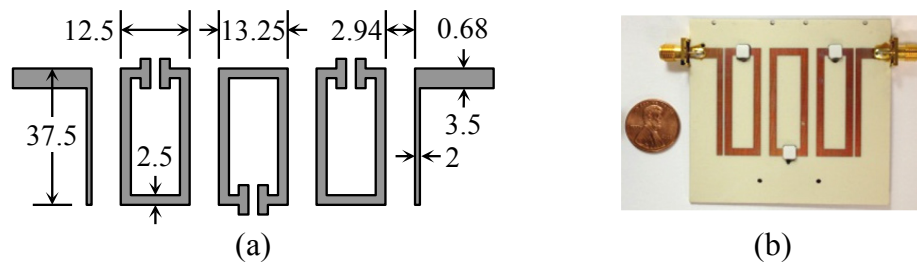
Figure 4-12: Third-order filter-limiter (a) layout and (b) fabricated device. (All units in mm)
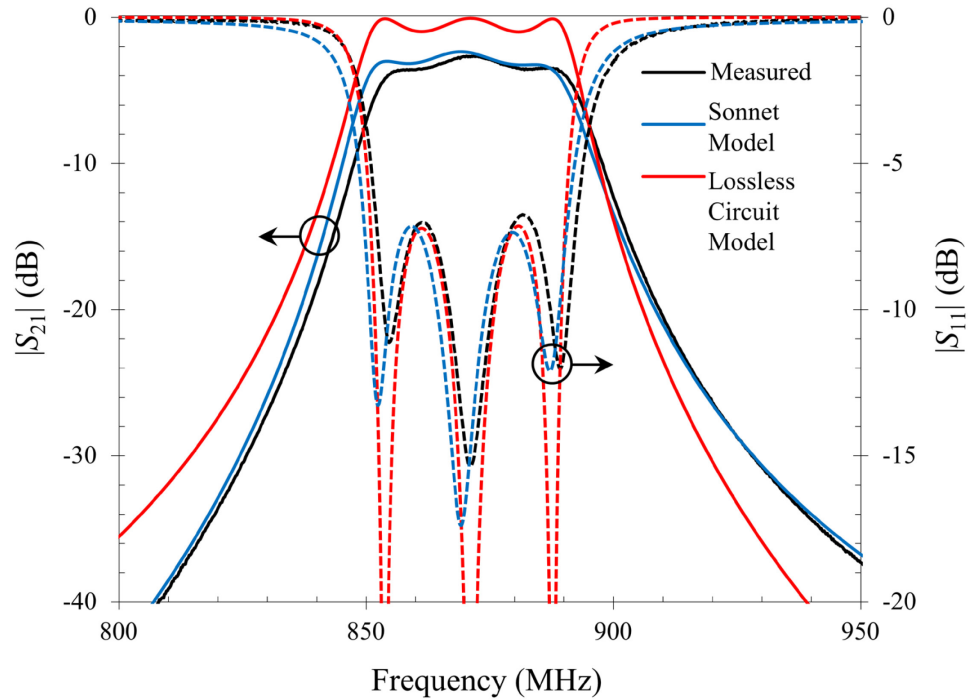
Figure 4-13: Third-order filter-limiter measured results agree with the Sonnet model and circuit theory.
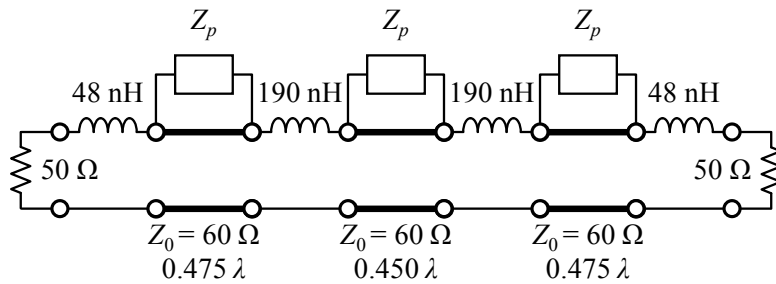
Figure 4-14: Third-order filter-limiter distributed circuit model.

input power increases, yielding a nearly flat response at maximum power. Attenuation increases significantly as input power increases from 43 to 53 dBm, coinciding with activation of the second plasma-shell in addition to the first. The transmission response is similar to the first-order case but with the added complexity of multiple plasma-shells that can activate independently.
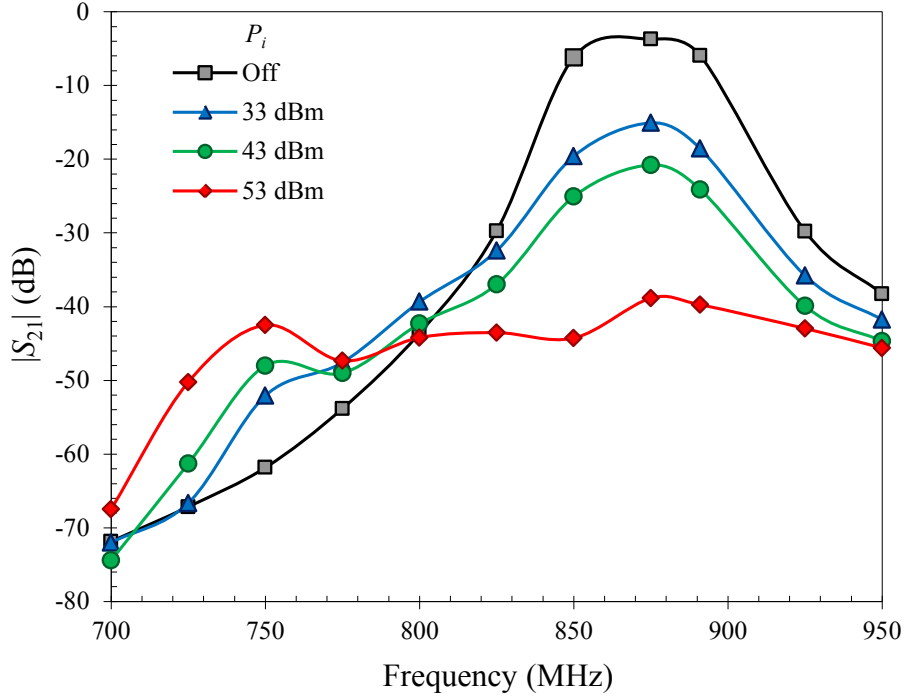
Figure 4-15: Third-order filter-limiter wideband measured results show disappearance of the passband as input power increases.

The effect of additional on-state plasma-shells is clearly seen in Figure 4-16, where the limiter transfer characteristic is measured using the test setup in Figure 4-8(c) at three frequencies: the lower band edge at 849 MHz, band center at 870 MHz, and midway at 860 MHz. The solid traces show passive "unprimed" operation where plasma-shells directly activate from incident power, and each frequency shows a unique characteristic curve with different slope, output level, and abrupt transitions where additional plasma-shells activate.

High output power and variable operation in the on state are undesirable, so a method was devised to eliminate this behavior. Plasma-shells were "primed" by an external voltage source to a very low plasma density using external keep-alive electrodes consisting of thin wires in contact with each shell. Low-level glow discharge provides a source of free electrons to initiate plasma discharge, reducing turn-on threshold voltage
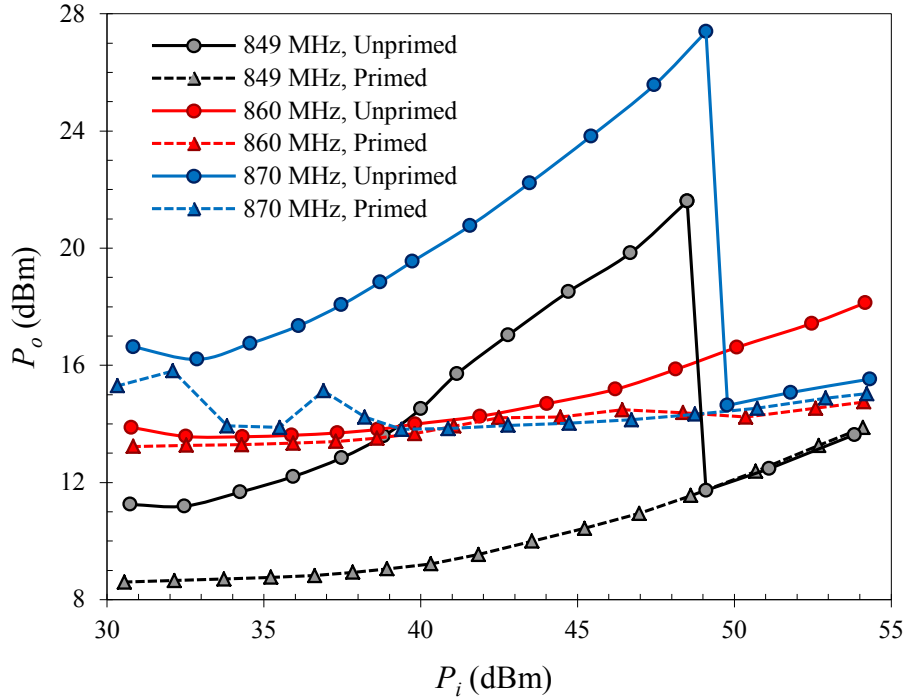
Figure 4-16: Third-order filter-limiter characteristic curve with input power at three frequencies in the passband. Unprimed operation is characterized by high output power and abrupt changes when additional plasma-shells activate, and primed operation shows lower output power and flatter slope.

and eliminating abrupt output power changes. This is a desirable alternative to traditional keep-alive electrodes that reduce operating lifetime of dc-coupled plasma devices, and avoids the use of radioactive materials [92]. Priming increased insertion loss by only 0.05 dB.

Reduced plasma-shell activation power is clearly demonstrated in Figure 4-17 where the input turn-on threshold power was recorded at each input drive frequency, along with resulting output power level. Priming reduced the average turn-on power in the passband from 29 to 20 dBm, and reduced resulting output power by 2 dB. Variation of turn-on and output power across the passband decreased by 1 dB, and the unprimed output power pedestal was eliminated.
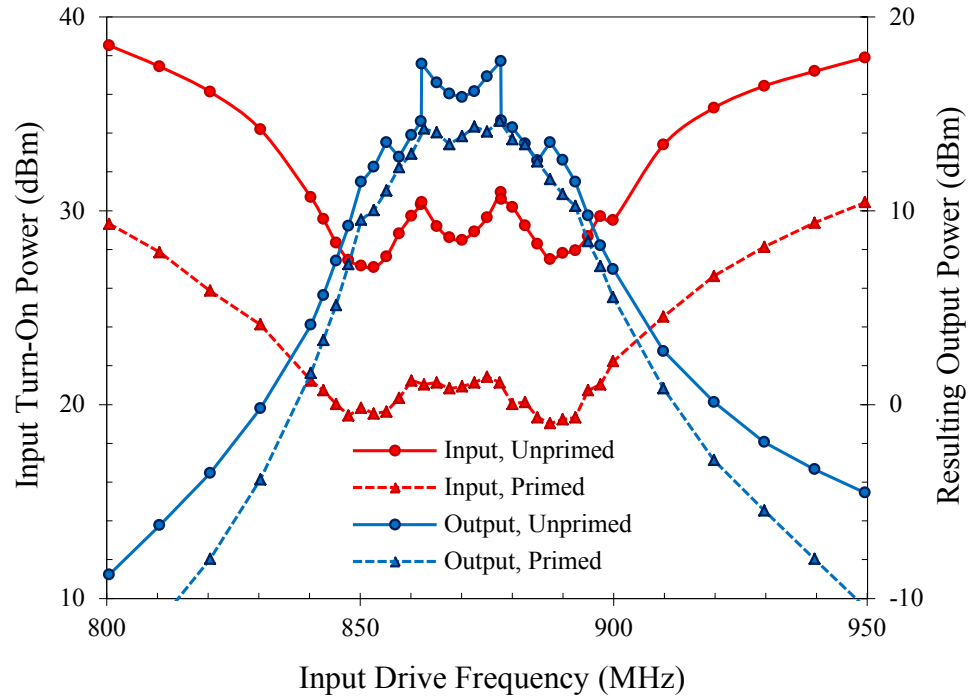
Figure 4-17: Third-order filter-limiter turn-on threshold power versus drive frequency, with output power at each turn-on level. Priming reduces turn-on threshold power and eliminates the output power pedestal from unprimed operation.

Third-order filter-limiter maximum attenuation while operating in the limiter region was predicted by the Sonnet model, first for one on-state plasma-shell by setting R_g to the critical value; critical attenuation is 17.0 dB for the first resonator, 11.1 dB for the second, and 16.8 dB for the third. Critical attenuation for the entire filter was considered with all plasma-shells at the critical point, resulting in 52.5 dB. This prediction is useful because it occurs well beyond the capability of the test system in which the highest measured attenuation at f_0 was 39.2 dB and was clearly operating in the limiter region with near-zero slope.

4.3 Conclusions

This chapter demonstrated a combined narrowband filter and HPM plasma limiter device composed of a traditional microstrip bent hairpin filter with discrete plasma-shells across resonator ends. Ac-coupled filter-limiter theory of operation and a plasma-shell equivalent circuit model were presented and validated with first-order filter-limiter measurements and EM simulation. A practical third-order filter-limiter demonstrated increased attenuation by cascading multiple resonators. Limiter performance was improved by priming the plasma-shells to a very low plasma density with an external voltage source without significantly increasing insertion loss.

Ac-coupled plasma-shells have application beyond HPM limiters; they can be used at different frequencies, other filter topologies, and entirely different microwave structures at low and high power levels, operating passively from incident microwave power or actively from priming voltage sources. This chapter presents new principles for using plasma-shells in planar microwave devices.

Chapter 5

Plasma Frequency Selective Surface

Several key challenges exist in creating large-scale plasma devices. First, plasma must be encapsulated in a way that maintains controlled gas composition, pressure, and purity. Second, power must be delivered to the plasma volume in a way that provides controlled EM properties across a frequency range of interest.

This chapter proposes a concept that addresses these challenges. Figure 5-1(b) shows a device consisting of rectangular plasma-shells in Figure 5-1(a) arranged in a

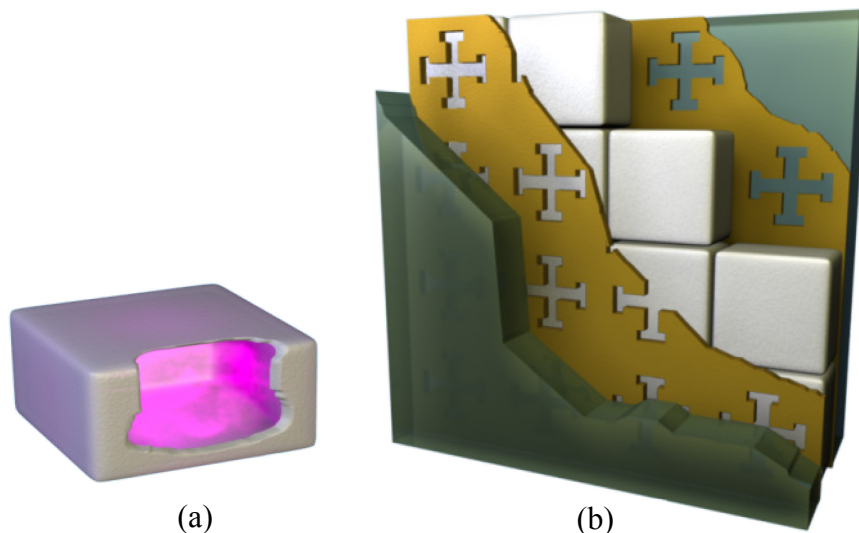(a)   (b)

Figure 5-1: (a) Plasma-shell cutaway showing internal plasma; (b) proposed switchable device made of patterned conductors around a plasma-shell array.

close-packed array that can be directly driven by high-voltage ac energy through conductive layers. These patterned layers are referred to as plasma excitation surfaces and are transparent to RF energy across a specified band.

This chapter is organized as follows: first, a novel plasma device is proposed in Section 5.1 that emulates the physical phenomenon of a large-scale plasma sheet in free space at X-band. The design of the electromagnetic structure is presented using full-wave simulation tools. Section 5.2 describes the fabrication and testing of the proposed device, and presents key measurements including passband frequency response in the off and on states, incidence angle sweep, and drive voltage sweep. Plasma parameters are estimated and ways to optimize the device are discussed. Finally, Section 5.3 summarizes results and describes potential applications of this technology.

5.1 Design and Fabrication

5.1.1 Proposed Concept

Electrical conductors in contact with plasma-shells are called plasma excitation surfaces; these must have large conductor area in contact with plasma-shells yet be transparent to one or more microwave bands. Some types of FSS elements have such properties. Each plasma excitation surface unit cell is an FSS element composed of a conductive sheet with etched slots. The Jerusalem cross pattern is employed in this device, but any shape can be used that meets the following criteria:

- bandpass response
- free-standing (i.e., no unconnected "floating" elements)
- large conductor coverage area

The FSS element pattern is repeated on the conductive surface on a closely-spaced regular grid. Plasma excitation surfaces are readily fabricated as single-sided PCBs. Two plasma excitation surfaces are laminated onto an array of plasma-shells slightly smaller than FSS elements. This composite material is energized with a high-voltage source to create a volume of plasma that directly interacts with propagating EM energy. Switchable transmission and reflection performance through the plasma volume is accomplished in this way.

The structure was designed to implement a second-order bandpass response in X-band and contain plasma-shells of size 4.23 mm × 4.23 mm × 2.24 mm with 176 μm wall thickness. The fill gas is 0.1% argon with balance of neon at 175 Torr.

5.1.2 Analysis

A candidate structure was optimized using full-wave simulation, and the resulting Floquet port model shown in Figure 5-2 is the unit cell of a symmetric second-order FSS with spacing of 6.35 mm. Floquet port simulation in HFSS models an infinite FSS array from a single unit cell with good speed. This model simulates one response from 5 to 18 GHz. Simplifications were made to the model to improve simulation time including flat conductors, merging plasma-shell electrodes with plasma excitation surfaces, and omitting shell side walls.

Inter-element coupling strength is primarily determined by FSS element spacing. Dense spacing of 0.21 λ at 10 GHz gives strong center frequency and bandwidth stability across scan angle. Element geometry provides several degrees of freedom for tuning center frequency and bandwidth and was adjusted so that an entire plasma-shell
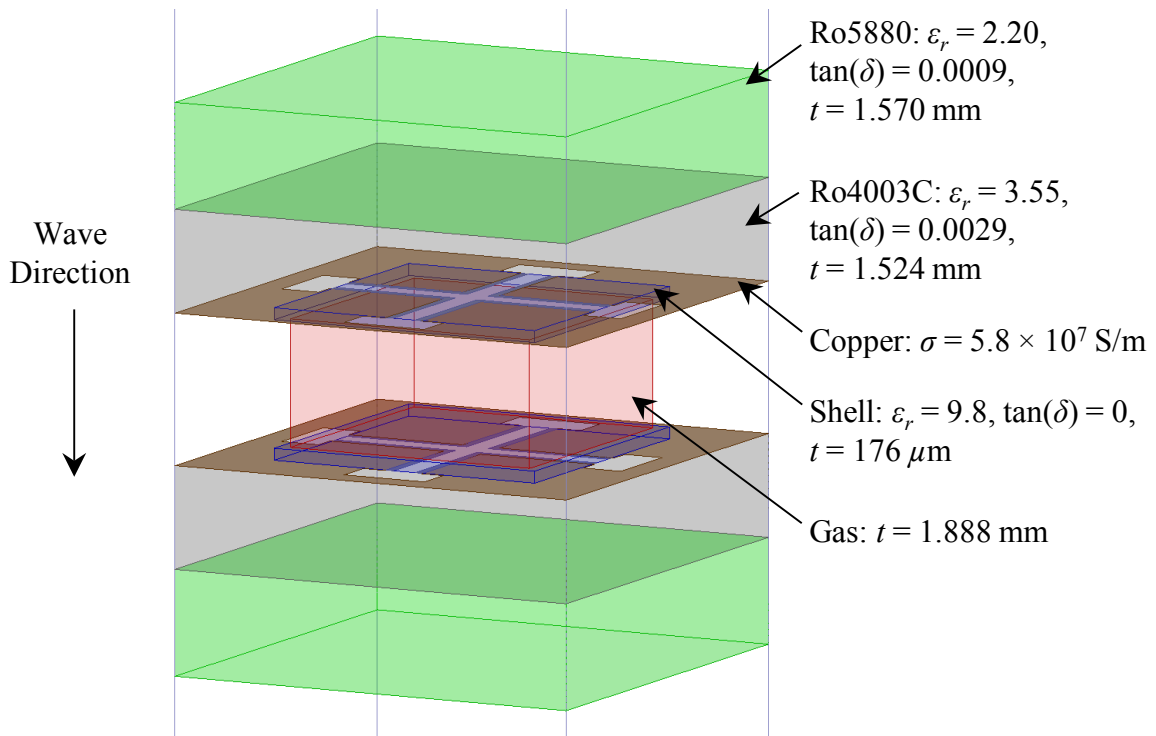
Figure 5-2: HFSS Floquet port model with material parameters and dimensions. The unit cell is composed of a single plasma-shell in the center surrounded by two single-layer PCBs, with outer dielectric slabs for port tuning.

could fit across the center cross-shaped slot to minimize performance deviation caused by placement error.

Outer dielectric slabs were added to increase port coupling strength for this structure in order to achieve sufficient return loss; the response was under-coupled without them. The dielectric is realized with commonly available unclad Rogers 5880 substrate material [93].

The simulated wideband response in Figure 5-3 shows center frequency of 10.1 GHz and bandwidth of 2.8 GHz. Insertion loss and return loss are 1.0 dB and 12.5 dB, respectively. The response of one single-sided Rogers 4003C PCB is shown for verification with measured results, and higher center frequency of 14.0 GHz is evident because electroded plasma-shells are not present to decrease element resonant frequency.
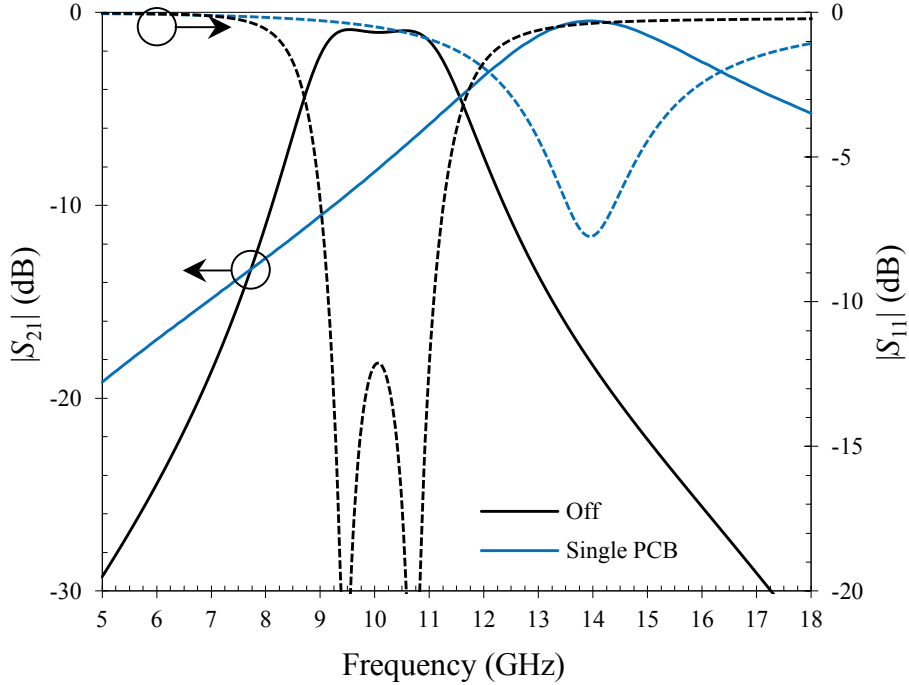
Figure 5-3: Simulation of proposed device shows good second-order off-state response, with return loss included for reference. One single-PCB response (without plasma-shell) is simulated for comparison with measured results.

5.1.3 Implementation

Fabricated PCBs in Figure 5-4 were made using standard photo-etching and plating processes. The top layer includes a finite 12 × 12 FSS array; this size was chosen because there were only 160 plasma-shells available for this experiment. The bottom layer is bare except for a perimeter copper flange filled with vias for continuous electrical contact with the mounting plate. One PCB was trimmed to 114 mm overall size for use as the top PCB.

The plasma-shell electroding and mounting process is shown in Figure 5-5 in which each shell was printed with electrodes on the top and bottom with cross-shaped shaped slots of width of 0.35 mm. To mechanically and electrically attach shells to the PCB, first an array of silver conductive epoxy dots were stenciled to the PCB, then shells

(a)   (b)
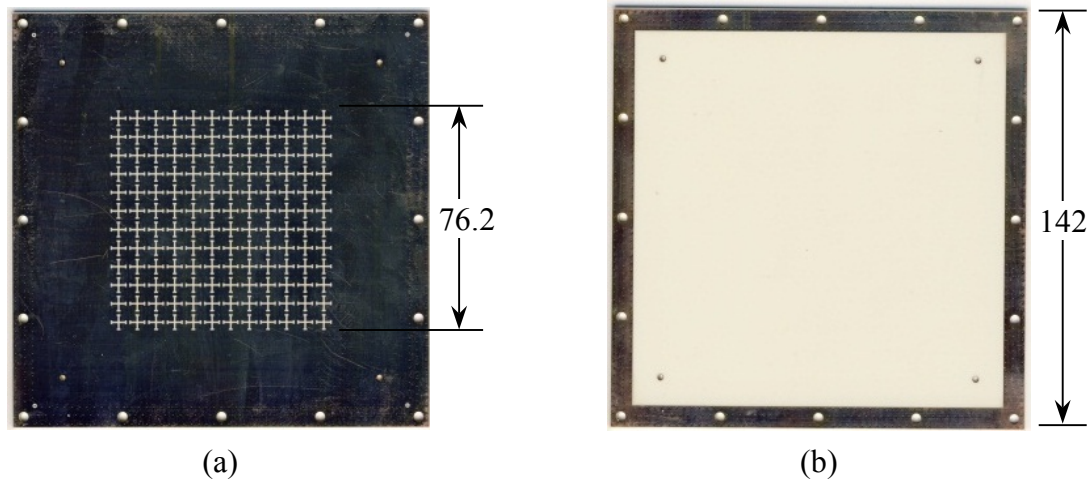
Figure 5-4: Fabricated PCB layers: (a) top plasma excitation surface with center 12 × 12 array and (b) blank bottom with perimeter flange for mounting plate ground continuity. (All units in mm)

(a)   (b)   (c)
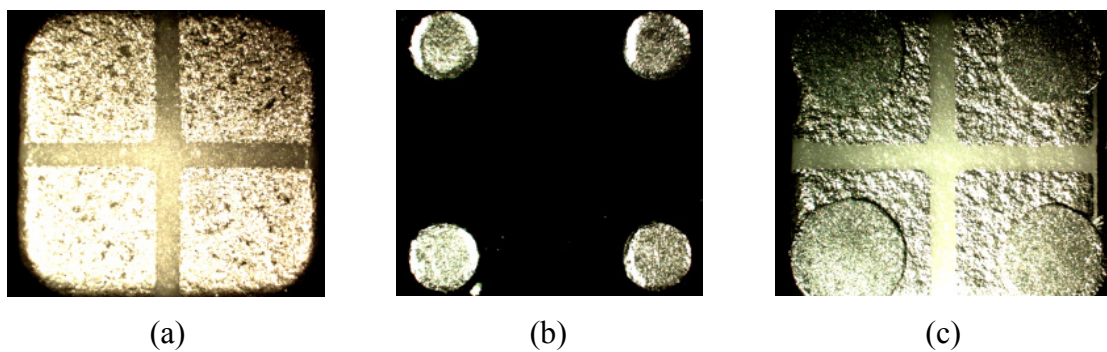
Figure 5-5: Plasma-shell assembly method where (a) conductive pads with cross-shaped slots were printed on top and bottom of each shell, (b) conductive epoxy dots were stenciled onto the PCB, and (c) each shell was placed onto the PCB, achieving optimal contact (fabrication trial seen through a glass slide pictured above).

were placed using a pick and place machine. To mount the second PCB to the array, silver epoxy dots were stenciled to the top PCB and placed on the bottom PCB/shell assembly. Alignment was maintained with alignment pins that were removed after the entire assembly was cured.

The assembled device is shown in Figure 5-6(a) without dielectric slabs. To mount the device to a large ground plane for testing, the bottom PCB (seen as the copper

border) was screwed to the mounting plate, and the seam was covered with aluminum tape. One sustainer output was connected to the mounting plate and the other to the top PCB that is isolated from the ground plane. The complete device is shown in Figure 5-6(b) with dielectric slabs taped in place to the top and bottom PCBs, and an orange glow is seen while the device is sustained at low voltage.

(a)   (b)
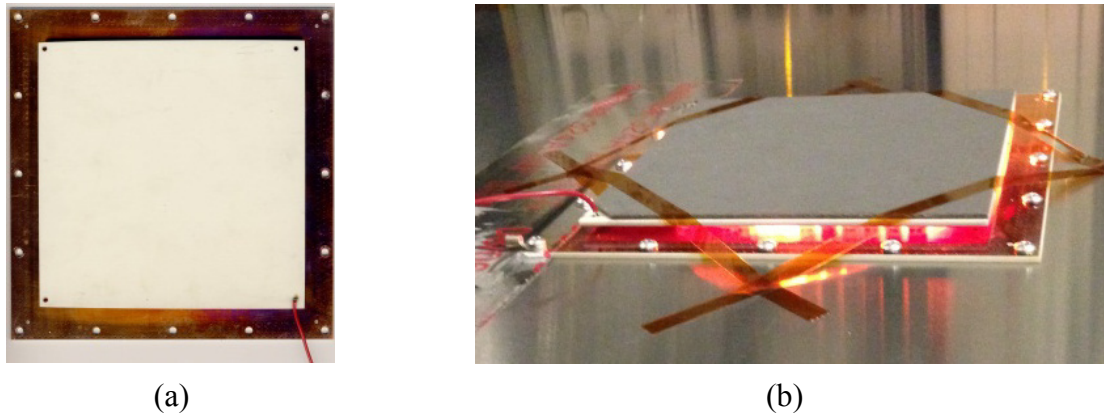
Figure 5-6: Assembled device (a) without dielectric slabs and (b) with dielectric slabs taped in place, showing weak plasma glow during initial turn-on test.

5.2 Experimental Results and Discussion

5.2.1 Test Setup

Device frequency response was measured with the test setup in Figure 5-7 in which a Rohde & Schwarz ZVB20 VNA measured transmission through the DUT for different plasma states and incidence angles. The DUT was mounted to a 610 mm (24 in) square plate that could be rotated, and the plate was substituted with reference plates for calibration. Two 2–18 GHz quad-ridge horns were placed in the far field for uniform illumination. Plate edge effects and small sample size limited useful measurement range to ~7–18 GHz.
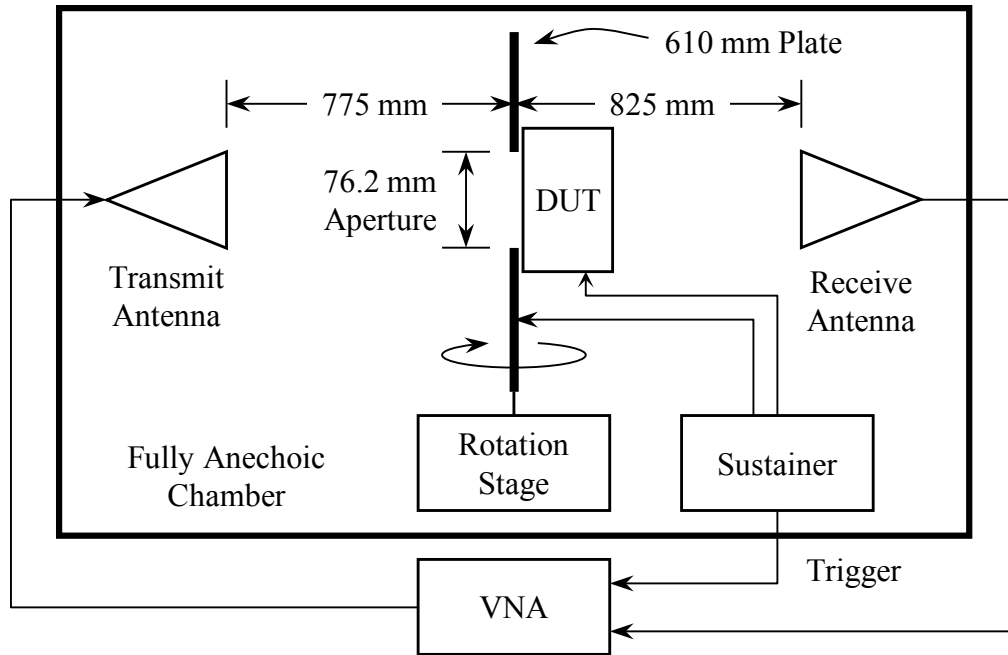
Figure 5-7: Test setup for transmission response measurement from 5 to 18 GHz with incidence angle sweep.

Figure 5-8(a) shows the actual measurement setup where the 610 mm plate is seen in the center, shown covered with absorber for a calibration measurement. The sustainer (not seen) is mounted on the far side of the Styrofoam column out of antenna line of sight, and the column and sustainer are rotated to sweep incidence angle. The DUT is mounted on the rear side of the plate in Figure 5-8(b), and high-intensity orange light is emitted during on-state operation.

The sustainer used here is a high-voltage square wave generator capable of bridged output drive of 1500 V_{pp} at 1 MHz, using a bipolar H-bridge scheme commonly used in PDP sustainer circuits [94], with energy recovery to recover capacitive displacement current for increased drive efficiency [95], [96]. This particular sustainer was not designed for continuous operation so all test data were measured with 10 millisecond drive bursts at a repetition rate of 4 bursts per second, and the VNA was

(a)
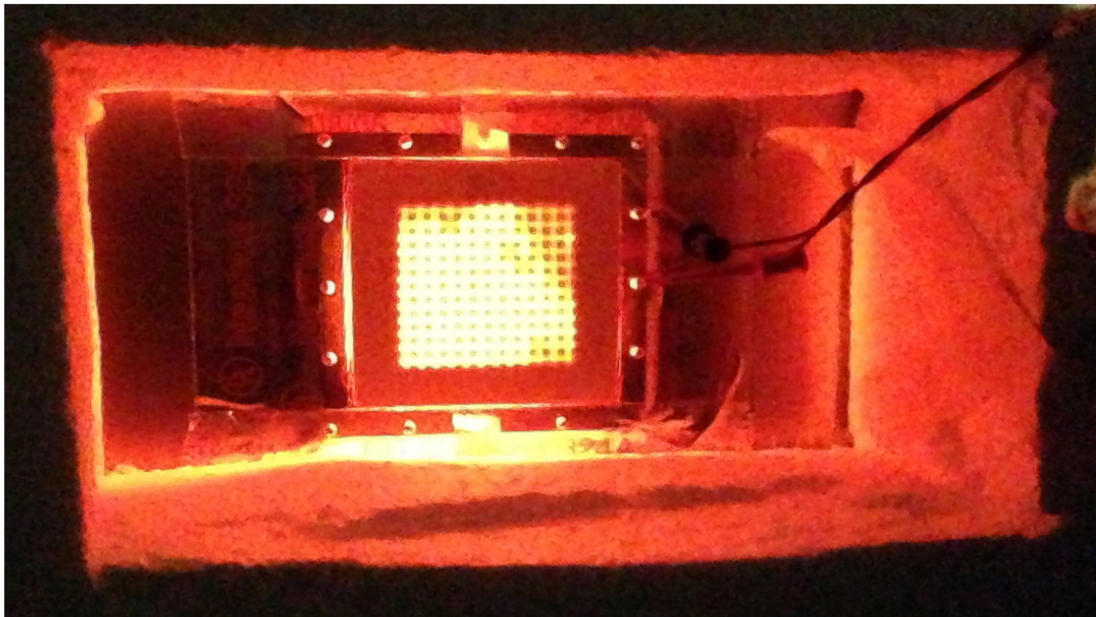
(b)

Figure 5-8: (a) Anechoic chamber test setup with two horns and 610 mm plate on center rotation stage; and (b) high-voltage device testing without dielectric slabs. Intense plasma-shell light is seen *through* the 1.524-mm-thick PCB substrate.

triggered to capture data within this large on-state window. This does not affect measurements because plasma attains steady-state operation on extremely short time scales. The test device is capable of continuous operation, limited only by the attached PCB maximum operating temperature.

Measurement data were time gated with a 2 nanosecond gating window to eliminate multipath and were referenced to a measured 76.2 mm aperture plate through-calibration. The small sample size manifests some measurement challenges including surface waves, impedance discontinuities at array edges, and aperture resonances, none of which were accounted for in post-processing. However, measured results are sufficient for conceptual validation. To accommodate such challenges, fabrication of a larger device is advised for precise measured results.

5.2.2 Wideband Results

The device in the off and on states and a single bare PCB (i.e., without plasma-shells) were measured for verification with the HFSS model. Measured results in Figure 5-9 show off-state center frequency of 11.0 GHz, bandwidth of 4.2 GHz, and minimum insertion loss of 5.1 dB. On-state center frequency increases to 12.6 GHz, bandwidth reduces to 3.0 GHz, and minimum insertion loss increases to 9.2 dB. Absolute insertion loss is not likely to be accurate because of finite array effects and calibration error; however, the measured center frequency is expected to be reliable.

Off-state and single PCB measured results compare well with simulation results in which measured passbands are higher by 1.0 GHz. Nulls at the lower passband are not present in simulation; this suggests that the measured nulls are artifacts of the finite array.
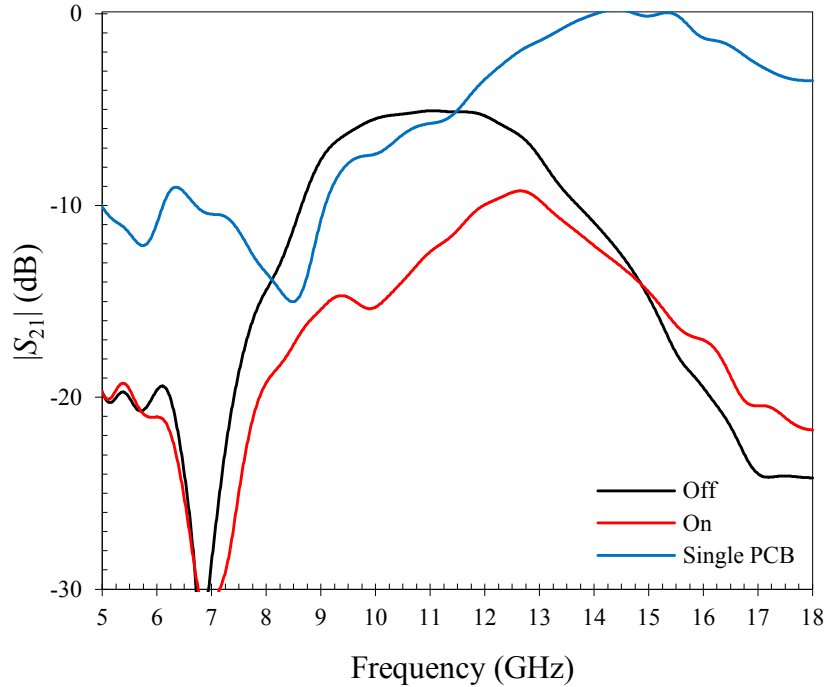
Figure 5-9: Measured wideband transmission response of the device in the off and on states driven at 1200 V_{pp}, 1 MHz, and normal incidence. Off-state and single PCB responses agree with the HFSS model. Measured data may only be useful above the nulls at 7 and 8.5 GHz that do not appear in simulation.

The on-state response has two important characteristics versus the off-state response: higher center frequency and higher insertion loss. The frequency shift is confirmed by the on-state response being higher than the off-state response above 15 GHz, and these characteristics will be examined more closely during plasma modeling in Section 5.2.5.

5.2.3 Incidence Angle Sweep

The device was measured in the off and on states as incidence angle was increased from normal (0°) to 60° in increments of 15°, shown in Figure 5-10. Center frequency and bandwidth appear relatively stable up to 45°, but either the device
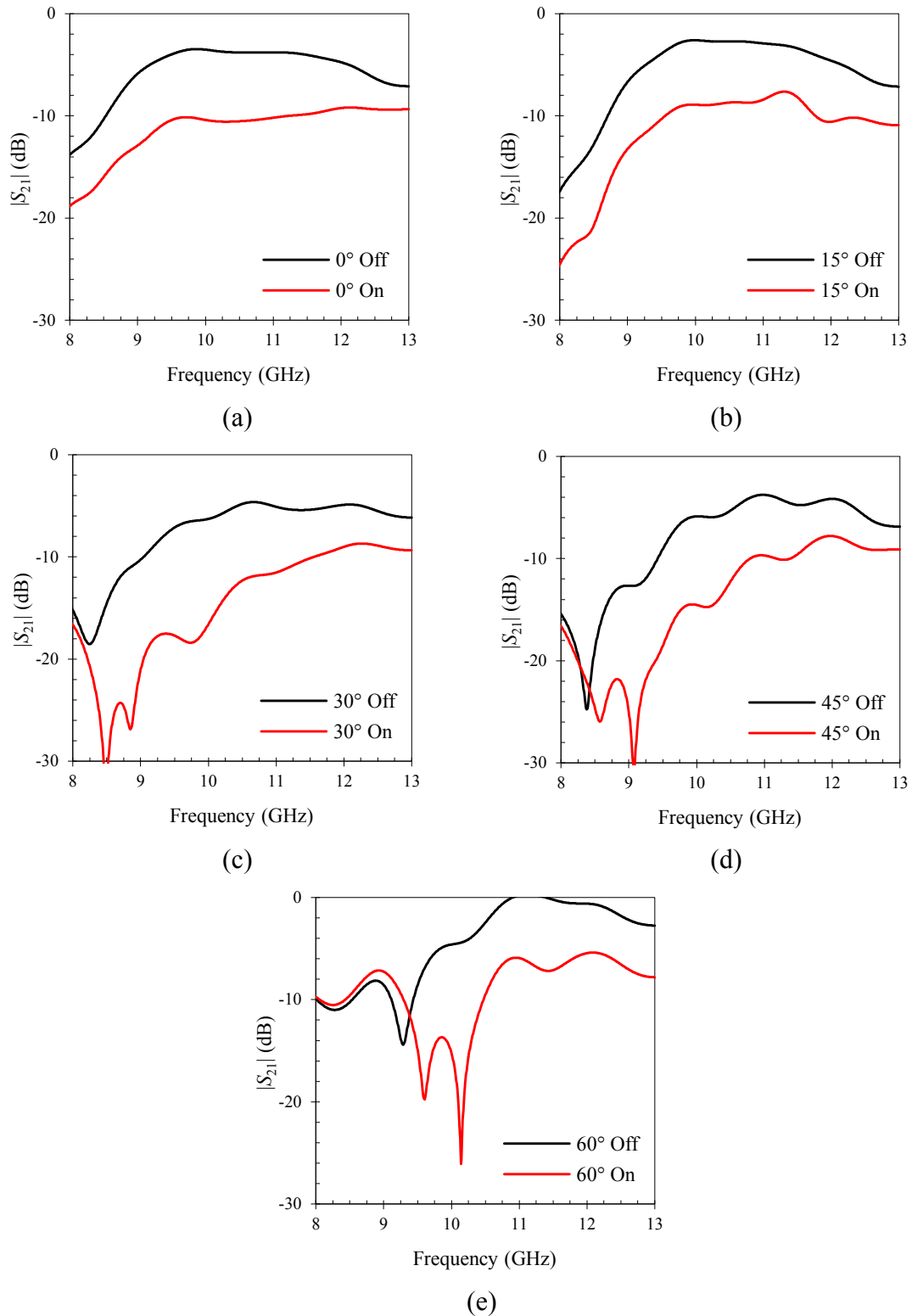
Figure 5-10: Measured transmission response in the off and on states versus incidence angle driven at 1200 V_{pp}, 1 MHz. Center frequency and bandwidth are stable at: (a) 0°; (b) 15°; (c) 30°; and (d) 45°. The device or test setup falls apart at (e) 60°. Switchable attenuation is significant across the passband at all angles.

performance or the measurement setup falls apart at 60° with insertion loss reaching an unrealistically low value and nulls moving near passband center.

Key design features such as electrically small and closely spaced FSS elements, and low-dielectric-constant slabs on the outer surfaces contribute to scan angle stability. With taller plasma-shells it is possible to design a device that meets the theoretical criterion for an optimally scan-independent FSS.

5.2.4 Drive Voltage Sweep

Increasing drive voltage has a significant effect on passband attenuation. Figure 5-11 shows that for each voltage increase of 200 V, average on-state passband attenuation
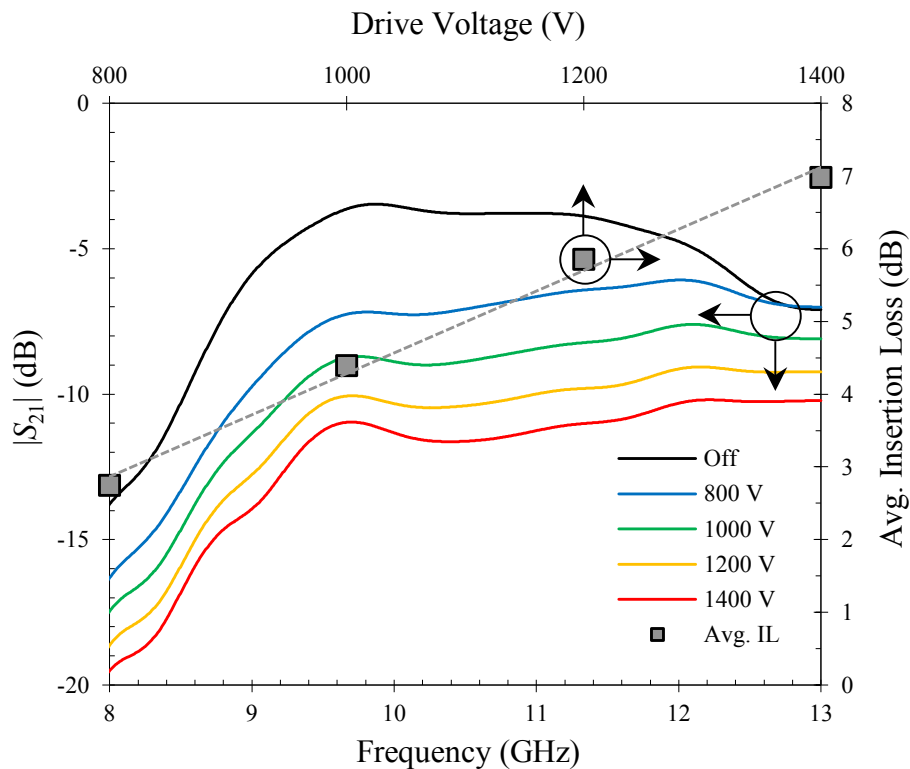
Figure 5-11: Measured transmission response in the off and on states with swept drive voltage at 1 MHz and normal incidence. Increasing drive voltage increases attenuation by 1.4 dB per 200 V. Maximum average passband attenuation is 7.0 dB at 1400 V_{pp}.

increases by 1.4 dB. Following the observed trend, an improved sustainer that outputs 2400 V_{pp} would more than double switchable attenuation from 5.9 dB at 1200 V_{pp} to 14.2 dB. This experiment likely indicates that increasing drive voltage directly increases electron density and gas conductivity, thereby increasing attenuation.

5.2.5 Plasma Medium Model

Measured results verify that the device provides significant switchable attenuation. To better understand the interaction between the device structure and plasma medium, the plasma volume can be modeled as a homogenous conductive dielectric medium. Complex permittivity (ε) is defined as $\varepsilon = \varepsilon_0(\varepsilon_r' + j\varepsilon_r'')$ and consists of real and imaginary relative permittivity (ε_r' and ε_r'' respectively). Both frequency-dependent components for a cold, collisional, and weakly ionized plasma are defined as

$$\varepsilon_r' = 1 - \frac{\omega_p^2}{\omega^2 + v^2} \text{ and}$$

(5.1)

$$\varepsilon_r'' = \frac{\omega_p^2 v/\omega}{\omega^2 + v^2}.$$

(5.2)

As can be seen, (5.1) and (5.2) are functions of plasma frequency (ω_p, in rad/s), microwave drive frequency (ω, in rad/s), and electron collision frequency (v, in rad/s) [62]. Loss tangent is defined as

$$\tan(\delta) = \frac{\omega\varepsilon_0\varepsilon_r'' + \sigma}{\omega\varepsilon_0\varepsilon_r'}$$

(5.3)

with frequency-independent gas conductivity (σ, in S/m) [97]. Plasma frequency is a function only of electron density (n_e, in cm^{-3}) given as

$$\omega_p = \sqrt{\frac{n_e e^2}{\varepsilon_0 m_e}} \tag{5.4}$$

with constants of elementary charge ($e = 1.6 \times 10^{19}$ C) and electron mass ($m_e = 9.1 \times 10^{-31}$ kg). Equation (5.4) simplifies to $56\,500\sqrt{n_e}$.

Gas number density (N, in cm^{-3}) is calculated from the ideal-gas equation of state and evaluates to 5.6×10^{18} cm^{-3} for plasma-shells used in this device at 300 K. Electron collision frequency is a function of gas pressure for noble gas plasmas and is available for electron temperature (T_e) of 300 K in Table 5.1 from [85], and for higher T_e in [98]. For plasma-shells used in this device, $v = 4.3 \times 10^9$ rad/s.

Table 5.1: Momentum-transfer collision rate for noble gases.

Gas	v/N (cm^3/s)
He	7.6×10^{-9}
Ne	7.6×10^{-10}
Ar	2.2×10^{-9}
Kr	1.8×10^{-9}
Xe	5.3×10^{-8}

To calculate ε, first n_e must be estimated which is possible with the HFSS model by simulating the on-state frequency shift proportional to n_e. The resulting value of 3.6×10^{12} cm^{-3} produces a frequency shift of 1.5 GHz that matches measured results. Calculated plasma frequency is 17.1 GHz, and calculated values for ε_r' and tan(δ) at 10 GHz are −1.88 and 0.105 respectively. Conductivity shifts the on-state response down, and a simulated value of 0.45 S/m matches the measured off-to-on-state increase in minimum insertion loss of 4.2 dB.

The transmission response of the HFSS model with plasma modeled as a frequency-dependent complex permittivity medium is shown in Figure 5-12. The shape

of the simulated on-state transmission response agrees with measured results in Figure 5-9, particularly with increased passband frequency and attenuation in the on state, validating the complex permittivity plasma model.
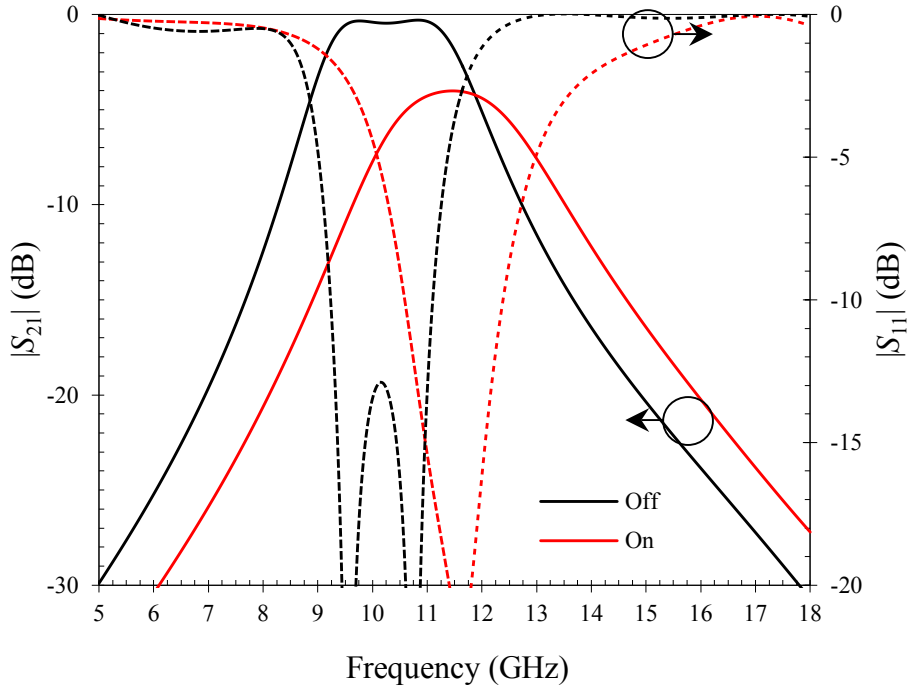
Figure 5-12: HFSS device simulation in off and on states, with plasma properties of $n_e = 3.6 \times 10^{12}$ cm^{-3}, $v = 4.3 \times 10^9$ rad/s, and $\sigma = 0.45$ S/m at normal incidence.

5.2.6 Power Usage

Device power usage was measured to be approximately 150 W (i.e., power density of 25 kW/m^2) by measuring sustainer input power with and without the device connected while operating at 1200 V$_{pp}$ and 1 MHz. This value does not measure sustainer conversion efficiency which is assumed to be high. Plasma power dissipation per unit volume can be estimated for noble gas plasmas dominated by two-body recombination by

$$P/V = kn_e^2 \Phi_i e \quad (\text{W/cm}^3) \tag{5.5}$$

where k is the two-body dissociative rate constant and Φ_i is the energy required to ionize a gas using an electron (E)-beam. Both constants are available for noble gases in Table 5.2 [85]. For plasma-shells used in this device with gas volume of 0.0284 cm^3 each and n_e estimated previously, predicted device power usage is 55 W (i.e., power density of 9.3 kW/m^2).

Table 5.2: Dissociative recombination rate constant and E-beam impact ionization potential for noble gases.

Gas	k (cm^3/s)	Φ_i (eV)
He	1.0×10^{-8}	41.5
Ne	1.8×10^{-7}	36.2
Ar	9.1×10^{-7}	26.2
Kr	1.6×10^{-6}	24.3
Xe	2.7×10^{-6}	21.9

Drive power can be dramatically reduced by using helium gas with a much lower rate constant due to order-of-magnitude longer plasma lifetime. Predicted power density drops by a factor of 16 (i.e., to 0.6 kW/m^2). The most significant driver of power usage is electron density, which should not be higher than needed. Further power reduction may be achieved by reducing total plasma volume. An example of this is locating smaller plasma-shells in the center of each FSS element where there is strongest EM interaction, not wasting power in areas of low RF coupling.

Large-area plasma devices clearly require significant, but not impractically large, power sources. Delivery of ac power in the 1 kV range at high frequency is practical with class E amplifiers that can operate at tens of megahertz at > 90% efficiency [99]. Supplies can achieve high power density and can scale up to arbitrarily high power levels. This is a practical power solution for mobile platforms, versus alternative approaches using lasers, E-beams, and pulsed high-voltage supplies.

5.3 Conclusions

This chapter presented a novel concept for RF-plasma interaction in a scalable plasma-shell device. The proposed X-band switched plasma device was fabricated and measured, showing good scan angle independence and significant attenuation in the passband. There are many other avenues for increasing attenuation such as plasma-shell optimization (e.g., gas mixture, gas pressure, shell size, and electrode geometry), waveform optimization (e.g., voltage and frequency), and structural optimization (e.g., plasma excitation surface geometry and additional layers).

This concept has the potential to be scaled for use in mobile systems. Power dissipation can be reduced over an order of magnitude with gas optimization and structural changes. Power sources can produce high-voltage and high-frequency waveforms with maximum efficiency and power density. The proposed concept can be very lightweight; the structure is composed primarily of hollow shells and dielectric material. Foams and dielectrics with engineered voids are often used in FSS construction because many designs require low-dielectric-constant materials [100]. Conformal structures are also possible that follow contours of space-constrained platforms.

Potential applications of large-area switchable plasma-shell devices include: active radomes, switchable EM apertures, and plasma metamaterials. This concept is an important first step for practical large-scale plasma devices to overcome traditional limitations concerning encapsulating and driving large plasma volumes.

Chapter 6

Conclusions and Future Work

6.1 Summary

The goal of this dissertation was to demonstrate narrowband front-end components that are hardened against HPM damage for civilian microwave systems. With the widespread use of microwave technologies in modern electronic devices, it is critical to protect these largely unprotected devices from intentional and unintentional destruction. This dissertation shows that several key components in the RF front end can be hardened without degrading performance or increasing cost.

The first component proposed in Chapter 3 is a band-select filter, a common component in receiver signal chains that prevents receiver degradation caused by high-power out-of-band interference. An evanescent-mode SIW combline topology was selected for analysis because it is a fully-insulated structure that resists internal voltage breakdown, has good unloaded Q-factor, and is easily implemented in low-cost PCBs. The contribution of this chapter is the demonstration of significant size reduction by cutting the cavity structure in half. The half-mode structure does not significantly radiate, and this is verified by full-wave simulation and experimental measurement. This structure

provides several benefits for civilian systems. First, filters can be designed with higher selectivity to reject more out-of-band energy because of the high-Q evanescent-mode cavity structure. Second, valuable substrate area is saved by the significant size reduction. Finally, the half-mode structure remains fully insulated against voltage breakdown during high-power transients.

The next component proposed in Chapter 4 is the plasma-shell filter-limiter, which was implemented as a low-cost microstrip bent hairpin filter. Theory was presented for a first-order filter-limiter with an ac-coupled limiter element, and it predicts two modes of operation: a limiter region where output power is clamped to a fixed value, and an attenuator region where the device acts as a fixed attenuator at high power. Theory also predicts that plasma-shell gas conductivity provides significant lossy loading and re-tunes the resonator to a lower frequency, and both effects are responsible for the limiting behavior. A simple plasma-shell equivalent circuit model was presented consisting of lumped elements, and model values were derived from measurements of a first-order device. Theory was confirmed by experimental measurements and simulated results.

The filter-limiter concept was demonstrated in practical form as a third-order bent hairpin filter-limiter. Interaction between multiple resonators and plasma-shells leads to behavior more complex than the first-order case, and this was evident in experimental measurements of the limiter characteristic curves. Turn-on threshold power was reduced by lightly priming the plasma-shells, and this barely increased insertion loss. The contribution of this chapter is the successful proof-of-principle demonstration of a low-cost integrated filter-limiter. The benefit to civilian systems is the addition of high-power plasma limiter functionality without significant increase in insertion loss, cost, size, or

weight. In addition to these benefits, the plasma-shell filter-limiter may reduce or eliminate the need for other protection devices in a microwave system and will operate with unlimited lifetime unlike conventional dc-coupled plasma devices.

The final component proposed in Chapter 5 is a plasma-shell FSS that functions as a switchable aperture to EMR propagating through free space. It can prevent HPM energy from entering the RF front end and is suitable for integration into a radome surrounding an antenna. Gas plasma has been known for decades to provide significant RF interaction but is difficult to produce and maintain on large scales. The device was implemented as a second-order FSS with an array of plasma-shells as the inner layer, and measurements showed significant switchable attenuation and good bandpass filter performance. Operation in the active mode, as demonstrated in this dissertation, is particularly useful for systems in close proximity to high-power sources such as long-range radars and other pulsed-power microwave sources. The contribution of this chapter is the demonstration of a simple concept that produces a large-scale plasma slab that significantly interacts with propagating EMR and can be excited with a simple switched-mode voltage source. This benefits civilian systems in several ways. First, in-band and out-of-band HPM energy can be rejected before it enters the first component of the RF front end, and this is particularly important for very sensitive systems and very high-power threats. Second, it is implemented in a very low-cost structure; it can be simply two single-sided PCBs and inexpensive plasma-shells. Third, operation in the active mode is possible with compact and efficient power supplies, not bulky and expensive power sources used with other plasma devices. Finally, it can be integrated into an existing component – the radome – and is inherently lightweight.

It is worth noting that the plasma FSS will provide less protection than a discrete limiter or filter-limiter. There are several reasons for this, and it has important implications for overall system protection. First, FSS elements will create far lower E-field within plasma-shells for a given threat level compared to filter-limiter structures. This is because threat energy is distributed over a large area, and optimization of element geometry for limiting effectiveness is severely restricted. Second, filter selectivity is lower because FSS order is low. Finally, FSS bandwidth must be greater to account for center frequency changes over incidence angle, fabrication tolerances, and environmental effects. All these reasons conspire to reduce plasma FSS limiting effectiveness. While this means that plasma FSSs cannot be the only HPM protection device for a system, it can still provide significant out-of-band filtering and is ideal for protecting against the highest-power threats. Because the structure is exposed to lower power density and produces lower E-field within plasma-shells, it can survive much higher power levels while providing significant protection. It can be the first line of defense against the highest power levels and will reduce threat energy density for subsequent front-end components.

These research outcomes are an important step towards widespread adoption of HPM hardening solutions. The narrowband front-end components presented in this dissertation are promising because they provide narrowband filtering performance comparable to conventional devices and can be fabricated in low-cost planar form. The use of plasma-shells as an integral limiting device provides high-power protection with negligible impact on size, weight, and cost.

6.2 Future Work

There are many opportunities to extend the concepts introduced in this dissertation. The utility of these proof-of-principle devices can be demonstrated in other useful forms and practical issues can be resolved to enable use in real-world systems.

In Chapter 3, a third-order combline evanescent-mode HMSIW bandpass filter structure was presented. Filter response can be improved by adding transmission zeroes and this can be done without increasing size by adding capacitive coupling between adjacent resonators. This technique is used in machined cavity combline filters, and the same result can be achieved at low cost with PCB construction. The structure can also be applied to large filter arrays in which total area is a major concern. For example, filter banks, di-, tri-, and multiplexers are ideal for this structure because multiple cavities can be closely packed and can share adjacent cavity walls.

In Chapter 4, plasma-shells were used as surface-mounted limiter elements in a low-cost microstrip filter-limiter. This concept is valid for other filter topologies and should be demonstrated in high-Q structures to produce integrated filter-limiters with low loss and high performance. Examples include 3-D structures such as machined combline and interdigital filters, suspended stripline construction, and waveguide filters. For X-band and higher, a construction method similar to suspended stripline is possible to achieve very low-cost and high-performance filter-limiters. A half-wavelength resonator (e.g., square open loop resonator) fits entirely on the face of one plasma-shell, so a filter could be constructed simply by arranging plasma-shells on a ground plane.

Practical aspects of the plasma-shell filter-limiter should be addressed, and these relate primarily to active priming. First, the relationship between priming and turn-on

power threshold, insertion loss, noise, and activation time need to be clearly understood. Second, techniques to implement active priming need to be identified that allow controlled priming with minimal impact on system cost and performance. Finally, active priming introduces the capability of controlled attenuation. Some receiver systems use variable attenuators in the RF front end to increase dynamic range, so this provides further opportunity to increase system integration.

The theory derived in this chapter can be extended to other microwave structures that exhibit resonance and are exposed to HPM energy. The first front-end component to consider is the antenna. In this context, an antenna inherently provides some level of protection by rejecting energy outside its frequency response. Plasma-shells can provide protection within the frequency response if they can be placed across locations that develop high voltage during resonance. A simple example is the rectangular planar patch antenna, where both resonant modes can be suppressed by one plasma-shell placed between a patch corner and ground plane. Another front-end component that may provide opportunities for integral in-band limiting is the harmonic filter. Protection at multiple bands may also be possible with plasma-shells using specialized resonant structures. Finally, overall limiting effectiveness would be improved if a method were developed to place transmission zeros within the passband during on-state operation.

In Chapter 5, a second-order plasma FSS with controllable attenuation was demonstrated. This concept can be developed for two important applications: HPM protection and low-observable operation. For HPM protection, it would be important to demonstrate self-activating operation from incident HPM energy. The same principles apply as were explained for the filter-limiter: the device should have narrow bandwidth,

the resonant element should maximize the E-field gradient within the plasma-shell gas, and priming will improve the self-activation response.

Low-observable applications require control of reflected energy. There are several approaches that can be pursued in future research. First, it is possible to frequency-shift incident energy using a concept called the phase switched screen. Plasma-shells can be rapidly switched at megahertz frequencies, and the device effectively acts as a spread-spectrum reflector. Second, incident energy can be completely absorbed over a narrow bandwidth using plasma sheets that are approximately one-third wavelength thick. The demonstrated structure can achieve this with larger plasma-shells. Finally, total broadband absorption is possible using an electrically thick stackup of graded plasma layers. This idea can be implemented by extending the concept in Chapter 5 to a multi-layer structure where each layer is excited to a different plasma density. A different FSS configuration would be needed to minimize interaction with propagating EMR over wide bandwidth.

Finally, plasma analysis and optimization is an important objective for future work. Plasma physics is a complex discipline especially when considering dynamic interaction with EM energy. This dissertation uses simple assumptions in support of a first-order analysis of plasma effects. Comprehensive 3-D modeling of plasma dynamics would be helpful to gain insight into behavior at the plasma-shell and device level. This is possible using combined physics simulation tools that simultaneously model EM structures, HPM wave interaction, and the evolution of gas plasma discharges. This would allow accurate modeling of plasma devices and rapid exploration of the complete design space.

Further research will allow these novel concepts to be used in many practical applications. The vulnerability of civilian microwave systems can be cost-effectively reduced when the full potential of these concepts is realized.

References

[1] M. G. Bäckström and K. G. Lövstrand, "Susceptibility of electronic systems to high-power microwaves: Summary of test experience," *IEEE Trans. Electromagn. Compat.*, vol. 46, no. 3, pp. 396–403, Aug. 2004.

[2] J. Benford et al., *High Power Microwaves*, New York: Taylor & Francis, 2007.

[3] R. F. Bilotta, "Receiver protectors: a technology update," *Microw. J.*, vol. 40, no. 8, Aug. 1997.

[4] R. B. Standler, *Protection of Electronic Circuits from Overvoltages*, New York: John Wiley & Sons, 1989.

[5] D. C. Wunsch and R. R. Bell, "Determination of threshold failure levels of semiconductor diodes and transistors due to pulsed power voltages," *IEEE Trans. Nucl. Sci.*, vol. 15, no. 6, pp. 244-259, Dec. 1968.

[6] M. A. Holloway, "Characterization and modeling of high power microwave effects in CMOS microelectronics," Ph.D. dissertation, Univ. of Maryland, College Park, MD, 2010.

[7] M. Yu, "Power-handling capability for RF filters," *IEEE Microw. Mag.*, vol. 8, no. 5, pp. 88-97, Oct. 2007.

[8] D. Anderson et al., "Microwave breakdown in resonators and filters," *IEEE Trans. Microw. Theory Techn.*, vol. 47, no. 12, pp. 2549-2556, Dec. 1999.

[9]   B. C. Wadell, *Transmission Line Design Handbook*, Boston, MA: Artech House, 1991.

[10] L. G. Maloratsky, "Reviewing the basics of microstrip lines," *Microw. & RF*, pp. 79-88, Mar. 2000.

[11] D. M. Pozar, *Microwave Engineering*, 3rd ed., New York: Wiley Interscience, 2005.

[12] K. L. Kaiser, *Electromagnetic Compatibility Handbook*, Boca Raton, FL: CRC Press, 2004.

[13] G. F. Craven and C. K. Mok, "The design of evanescent mode waveguide bandpass filters for a prescribed insertion loss characteristic," *IEEE Microw. Theory Techn.*, vol. MTT-19, no. 3, pp. 295-308, Mar. 1971.

[14] B. A. Munk, *Frequency Selective Surfaces*, New York: Wiley Interscience, 2000.

[15] B. A. Munk, *Finite Antenna Arrays and FSS*, New York: Wiley Interscience, 2003.

[16] W. L. Nighan, "Electrical conductivity of partially ionized noble gases," *Phys. Fluids*, vol. 12, no. 1, pp. 162-172, Jan. 1969.

[17] *R. P. Pipeline: That's Life*, CPI Wireless Solutions, Beverly Microw. Div., Beverly, MA, Sep. 1996. [Online] Available: http://www.cpii.com/docs/related/4/TR%20 Life.pdf [Jan. 14, 2013].

[18] D. Deslandes and K. Wu, "Accurate modeling, wave mechanisms, and design considerations of a substrate integrated waveguide," *IEEE Trans. Microw. Theory Techn.*, vol. 54, no. 6, pp. 2516-2526, Jun. 2006.

[19] M. Almalkawi et al., "Dual-mode substrate integrated waveguide (SIW) bandpass filters with an improved upper stopband performance," *36th Int. Conf. on Infrared, Millimeter, and THz Waves*, Houston, TX, Oct. 2011.

[20] M. Almalkawi et al., "Magnetically tunable substrate integrated waveguide bandpass filters employing ferrites," *36th Int. Conf. on Infrared, Millimeter, and THz Waves*, Houston, TX, Oct. 2011.

[21] M. Almalkawi et al., "Design of a dual-band dual-mode substrate integrated waveguide filter with symmetric transmission zeros," *IEEE Appl. Electromagn. Conf.*, Kolkata, India, Dec. 2011.

[22] Z. C. Hao et al., "Compact super-wide bandpass substrate integrated waveguide (SIW) filters," *IEEE Trans. Microw. Theory Techn.*, vol. 53, no. 9, pp. 2968-2977, Sep. 2005.

[23] F. Xu and K. Wu, "Guided-wave and leakage characteristics of substrate integrated waveguide," *IEEE Trans. Microw. Theory Techn.*, vol. 53, no. 1, pp. 66-73, Jan. 2005.

[24] Y. Wang et al., "Half mode substrate integrated waveguide (HMSIW) bandpass filter," *IEEE Microw. Wireless Compon. Lett.*, vol. 17, no. 4, pp. 265-267, Apr. 2007.

[25] Z. G. Wang et al., "Half mode substrate integrated folded waveguide (HMSIFW) and partial H-plane bandpass filter," *Prog. Electromagn. Res.*, vol. 101, pp. 203-216, 2010.

[26] Q. Lai et al., "Characterization of the Propagation Properties of the half-mode substrate integrated waveguide," *IEEE Trans. Microw. Theory Techn.*, vol. 57, no. 8, pp. 1996-2004, Aug. 2009.

[27] Q. H. Lai et al., "Half-mode substrate integrated waveguide transverse slot array antennas," *IEEE Trans. Antennas Propag.*, vol. 57, no. 4, pp. 1064-1072, Apr. 2009.

[28] Y. Cheng et al., "Half mode substrate integrated waveguide (HMSIW) directional filter," *IEEE Microw. Wireless Compon. Lett.*, vol. 17, no. 7, pp. 504-506, Jul. 2007.

[29] B. Liu et al., "Half mode substrate integrated waveguide (HMSIW) 3-dB coupler," *IEEE Micro. Wireless Comp. Lett.*, vol. 17, no. 1, pp. 22-24, Jan. 2007.

[30] R. W. Rhea, *HF Filter Design and Computer Simulation*, Norcross, GA: Noble Publishing Corp., pp. 363-371, Jan. 1994.

[31] L. S. Wu et al., "Evanescent-mode bandpass filters using folded and ridge substrate integrated waveguides (SIWs)," *IEEE Microw. Wireless Compon. Lett.*, vol. 19, no. 3, pp. 161-163, Mar. 2009.

[32] X. Gong et al., "Precision fabrication techniques and analysis on high-Q evanescent-mode resonators and filters on different geometries," *IEEE Trans. Microw. Theory Techn.*, vol. 52, no. 11, pp. 2557-2566, Nov. 2004.

[33] E. Naglich et al., "Bandpass-bandstop filter cascade performance over wide frequency tuning ranges," *IEEE Trans. Microw. Theory Techn.*, vol. 58, no. 12, pp. 3945-3953, Dec. 2010.

[34] J. Lee et al., "Frequency response control in frequency-tunable bandstop filters," *IEEE Microw. Wireless Comp. Lett.*, vol. 20, no. 12, pp. 669-671, Dec. 2010.

[35] H. Sigmarsson, "Widely tunable, high-Q, evanescent-mode cavity filters: Fabrication, control, and reconfigurability," Ph.D. dissertation, Purdue Univ., W. Lafayette, IN, pp. 129-136, 2010.

[36] H. Joshi, "Multi-band RF bandpass filter design," Ph.D. dissertation, Purdue Univ., W. Lafayette, IN, pp. 92-106, 2010.

[37] R. Kaul, *Microwave Limiters*, Wiley Encyclopedia of Elect. and Electron. Eng., 2007.

[38] T. Nilsson, "Investigation of limiters for HPM and UWB front-door protection," M.S. thesis, Linköpings University, Sweden, 2006.

[39] B. M. Coaker et al., "High-power multi-function radar receiver protection," *Proc. 3rd EuRAD*, Manchester, UK, Sep. 2006.

[40] A. L. Ward et al., "Spike leakage and burnout of silicon PIN diode microwave limiters," Harry Diamond Laboratories, Adelphi, MD, Jun. 1991.

[41] H. Goldie, "Radar receiver protector with auxiliary source of electron priming," U.S. Patent 4 245 197, Jan. 13, 1981.

[42] L. T. Gritter et al., "Method and apparatus for providing a carbon nanotube plasma limiter having a sub-ns response time," U.S. Patent 20080165466A1, Jan. 5, 2007.

[43] *Receiver protector technology*, CPI Wireless Solutions, Beverly Microw. Div., Beverly, MA. [Online]. Available: http://www.cpii.com/docs/related/4/RP%20Tech %20Art.pdf [Jul. 30, 2012].

[44] P. E. Ferguson and R. D. Dokken, "A high power X-band receiver protector," *Int. Electron Devices Mtg.*, Dec. 1974.

[45] T. P. Carlisle, "X-band high-power multipactor receiver protector," *IEEE Trans. Microw. Theory Techn.*, vol. 26, no. 5, pp. 345-347, May 1978.

[46] N. J. Brown, "Control and protection devices," *Northeast Electronics Res. Eng. Mtg.*, vol. 1, pp. 106-115, Oct. 1974.

[47] S. Balevičius et al., "Fast protector against EMP using thin epitaxial and polycrystalline manganite films," *IEEE Electron Device Lett.*, vol. 32, no. 4, pp. 551-554, Apr. 2011.

[48] J. C. Booth et al., "A superconducting microwave power limiter for high-performance receiver protection," *IEEE Microw. Theory Techn.*, vol. 1, pp. 139-142, Jun. 2004.

[49] A. A. Abidi, "The path to the software-defined radio receiver," *IEEE J. Solid-State Circuits*, vol. 42, no. 5, pp. 954-966, May 2007.

[50] R. Tan and R. Levy, "A limiting filter for application in a GPS receiver," in *IEEE MTT-S Int. Microw. Sypm. Dig.*, 1993, vol. 2, pp. 881-883.

[51] R. Cory, "PIN-limiter diodes effectively protect receivers," *EDN*, pp. 50-64, Dec. 2004. [Online]. Available: www.edn.com/design/analog/4327757/pin-limiter-diodes -effectively-protect-receivers [Jan. 12, 2013].

[52] P. S. Taylor et al., "An active annular ring frequency selective surface," *IEEE Trans. Antennas Propag.*, vol. 59, no. 9, pp. 3265-3271, Sep. 2011.

[53] G. I. Kiani, "Passive, active, and absorbing frequency selective surfaces for wireless communication applications," Ph.D. dissertation, Macquarie Univ., Sydney, Australia, 2009.

[54] C. M. Rhoads et al., "Electronically tunable optical periodic surface filters with an alterable resonator frequency," U.S. Patent 5 619 365, Apr. 8, 1997.

[55] F. Bayatpur, "Meta-material inspired frequency-selective surfaces," Ph.D. dissertation, Univ. of Michigan, Ann Arbor, MI, 2009.

[56] B. Schoenlinner et al., "Switchable low-loss RF MEMS Ka-band frequency-selective surface," *IEEE Trans. Microw. Theory Techn.*, vol. 52, no. 11, pp. 2474-2481, Nov. 2004.

[57] E. A. Parker and S. Massey, "Application of FSS structures to selectively control the propagation of signals into and out of buildings," ERA Rep. 2004-0072 A5, ERA Techn., Surrey, UK, Mar. 2004.

[58] S. Pugh, "Using FSS in HPM applications," M.S. thesis, Air Force Inst. of Techn., Dayton, OH, 2010.

[59] M. Bäckström et al., "Can intentional electrical discharges be used for HPM protection?," *IEEE Symp. Electromagn. Compat.*, Rome, Italy, pp. 752-757, Aug. 2011.

[60] P. Hindle, "The state of RF/microwave switch devices," *Microw. J.*, vol. 53, no. 11, pp. 20-36, Nov. 2010.

[61] M. P. Bachynski, "Electromagnetic wave penetration of reentry plasma sheaths," *URSI*, vol. 96D, no. 2, pp. 147-154, Feb. 1965.

[62] J. P. Rybak, "Causes, effects and diagnostic measurements of the reentry plasma sheath," Rep., Colorado State Univ., Fort Collins, CO, Dec. 1970.

[63] R. A. Hartunian, "Causes and mitigation of radio frequency (RF) blackout during reentry of reusable launch vehicles," Rep. ATR-2007(5309)-1, Aerospace Corp., El Segundo, CA, Jan. 2007.

[64] G. Bin and W. Xiaogang, "Power absorption of high frequency electromagnetic waves in a partially ionized plasma layer in atmosphere conditions," *Plasma Sci. Techn.*, vol. 7, no. 1, Feb. 2005.

[65] W. W. Destler et al., "Experimental studies of high-power microwave reflection, transmission, and absorption from a plasma-covered plane conducting boundary," *J. Appl. Phys.*, vol. 69, no. 9, pp. 6313-6318, May 1991.

[66] C. S. Gürel and O. Emrah, "Reduction of reflection from conducting surfaces using plasma shielding," in *Electromagn. Waves*, InTech, Rijeka, Croatia, pp. 449-470, Jun. 2011.

[67] U. Jordan et al., "Microwave breakdown in slots," *IEEE Trans. Plasma Sci.*, vol. 32, no. 6, pp. 2250-2262, Dec. 2004.

[68] R. S. Smith et al., "Gas-breakdown transmit-receive tube turn-on times," *IEEE Trans. Plasma Sci.*, vol. PS-14, no. 1, pp. 63-66, Feb. 1986.

[69] H. Shapiro, "Electromagnetic scattering properties of a resonant plasma," Ph.D. dissertation, California Inst. of Techn., Pasadena, CA, 1956.

[70] H. M. Musal, "On the theory of the radar-plasma absorption effect," GM Defense Res. Laboratories, Santa Barbara, CA, Jul. 1963.

[71] T. Anderson et al., "Plasma frequency selective surfaces," *IEEE Plasma Sci.*, vol. 35, no. 2, Apr. 2007.

[72] J. C. Vardaxoglou, "Optical switching of frequency selective surface bandpass response," *IEEE Electronics Lett.*, vol. 32, no. 25, pp. 2345-2346, Dec. 1996.

[73] D. P. Murphy et al., "X-band microwave properties of a rectangular plasma sheet," Interim Rep., Naval Res. Lab, Washington, DC, May 1999.

[74] S. Larigaldie and L. Caillault, "Dynamics of a helium plasma sheet created by a hollow-cathode electron beam," *J. Appl. Phys.*, vol. 33, pp. 3190-3197, Jul. 2000.

[75] Y. S. Zhang and J. E. Scharer, "Plasma generation in an organic molecular gas by an ultraviolet laser pulse," *J. Appl. Phys.*, vol 73, no. 10, pp.4779-4784, Jan. 1993.

[76] K. L. Kelly et al., "Laser ionization and radio frequency sustainment of high-pressure seeded plasmas," *J. Appl. Phys.*, vol. 92, no. 2, pp. 700-709, Jul. 2002.

[77] *RO4000 series high frequency circuit materials*, Rogers Corp., Rogers, CT. [Online]. Available: http://www.rogerscorp.com/documents/726/acm/RO4000-Laminates---Data-sheet.aspx [Nov. 1, 2012].

[78] ANSYS HFSS, www.ansys.com/products/simulation+technology/electromagnetics/high-performance+electronic+design/ansys+hfss/

[79] X. Liu et al., "High-Q tunable microwave cavity resonators and filters using SOI-based RF MEMS tuners," *J. Microelectromechanical Syst.*, vol. 19, no. 4, pp. 774-784, Aug. 2010.

[80] G. L. Matthaei et al., *Microwave Filters, Impedance-Matching Networks, and Coupling Structures*, Boston, MA: Artech House, 1980.

[81] E. G. Cristal and S. Frankel, "Hairpin-line and hybrid hairpin-line/half-wave parallel-coupled-line filters," *IEEE Trans. Microw. Theory Techn.*, vol. MTT-20, pp. 719-728, Nov. 1972.

[82] M. Sagawa et al., "Miniaturized hairpin resonator filters and their application to receiver front-end MIC's," *IEEE Trans. Microw. Theory Techn.*, vol. 37, no. 12, Dec. 1989.

[83] R. Levy et al., "Design of microwave filters," *IEEE Trans. Microw. Theory Techn.*, vol. 50, no. 3, pp. 783-793, Mar. 2002.

[84] J. Hong and M. J. Lancaster, "Couplings of microstrip square open-loop resonators for cross-coupled planar microwave filters," *IEEE Trans. Microw. Theory Techn.*, vol. 44, no. 12, pp. 2099-2109, Dec. 1996.

[85] R. J. Vidmar, "On the use of atmospheric pressure plasmas as electromagnetic reflectors and absorbers," *IEEE Trans. Plasma Sci.*, vol. 18, no. 4, pp. 733-741, Aug. 1990.

[86] Y. P. Raizer and J. E. Allen, *Gas Discharge Physics*, vol. 1, Berlin: Springer-Verlag, pp. 52-67, 1991.

[87] M. Lofgren et al., "Breakdown phenomena in microwave transmit-receive switches," *J. Appl. Phys.*, vol. 69, no. 4, pp. 1981-1992, Feb. 1991.

[88] F. M. Penning and C. C. Addink, "The starting potential of the glow discharge in neon-argon mixtures between large parallel plates," *Physica*, vol. 1, pp. 1007-1027, May 1934.

[89] D. L. Bitzer et al., "Gaseous display and memory apparatus," U.S. Patent 3 559 190, Jan. 26, 1971.

[90] D. G. Swanson, "Narrow-band microwave filter design," *IEEE Microw. Mag.*, pp. 105–114, Oct. 2007.

[91] Sonnet EM, www.sonnetsoftware.com/products/sonnet-suites/

[92] H. Goldie, "Radioactive (tritium) ignitors for plasma limiters," *IEEE Trans. Electron Devices*, vol. 19, no. 8, pp. 917-928, Aug. 1972.

[93] *RT/duroid 5870/5880 high frequency laminates*, Rogers Corp., Rogers, CT. [Online]. Available: http://www.rogerscorp.com/documents/606/acm/RT-duroid-5870-5880-Data-Sheet.pdf [Jan. 8, 2013].

[94] E. F. Peters, "Control apparatus for supplying operating potentials," U.S. Patent 3 959 669, May 25, 1976.

[95] B. K. Velayudhan et al., "Energy recovery in plasma display panel," U.S. Patent 6 917 351, Jul. 12, 2005.

[96] L. F. Weber et al., "Power efficient sustain drivers and address drivers for plasma panel," U.S. Patent 4 866 349, Sep. 12, 1989.

[97] C. A. Balanis, *Advanced Engineering Electromagnetics*, New York: John Wiley & Sons, 2012.

[98] P. Baille et al., "Effective collision frequency of electrons in noble gases," *J. Phys. B: Atomic Molecular Phys.*, vol. 14, pp. 1485-1495, May 1981.

[99] N. Mohan et al., *Power Electronics: Converters, Applications, and Design*, 3rd ed., New York: John Wiley & Sons, 2002.

[100] D. J. Kozakoff, *Analysis of Radome-Enclosed Antennas*, 2nd ed., Boston, MA: Artech House, 2010.